Cell cycle dynamics regulate H3K27 and H3K9 histone modifications

Liyne Nogay [1, 2], Ananthakrishnan Vijayakumar Maya § [1, 2], Lara Heckmann § [1, 2], Francesco Cardamone [1, 2, 3], Isabelle Grass [1, 4], Aakriti Singh [1, 2], Anna Frey [1, 5], Laurin Ernst [1, 2], Nicola Iovino [3, 4], Anne-Kathrin Classen [1, 4, *]

§ shared co-authors

* corresponding author: anne.classen@biologie.uni-freiburg.de

1 Faculty of Biology, University of Freiburg, Freiburg, Germany

2 International Max Planck Research School for Epigenetics, Biophysics and Metabolism, Freiburg, Germany

3 Max Planck Institute of Immunobiology and Epigenetics, Freiburg, Germany

4 CIBSS Centre for Integrative Biological Signalling Studies, University of Freiburg, Freiburg, Germany

5 Spemann Graduate School of Biology and Medicine (SGBM), University of Freiburg Germany

ABSTRACT

Cell cycle progression presents a fundamental challenge to genome integrity, particularly due to the need to reestablish post-translational histone modifications (PTMs) following DNA replication. Although proliferative and differentiating tissues exhibit markedly different cell cycle dynamics, how these differences shape the histone modification landscape in vivo remains largely unexplored. Here, we show that levels of H3K27ac, H3K27me3, and H3K9me3 are tightly linked to cell cycle dynamics in the *Drosophila* wing imaginal disc. We demonstrate that both physiological and pathological elongation of the cell cycle led to an accumulation of H3K9me3 and H3K27me3, whereas cell cycle acceleration reduces their levels. In contrast, H3K27ac exhibits the opposite pattern: levels decrease in arrested cells and increase with faster cycling. Genome-wide CUT&Tag analysis reveals that these changes predominantly affect genomic loci already modified in normally proliferating tissue. Importantly, the regulation of methylation levels at H3K9 and H3K27 is not solely mediated by the cell cycle machinery but reflects a metabolically guided process in which the rate of methylation is coupled to the rate of cell proliferation through metabolic activity, including signaling via the Insulin/PI3K/Akt pathway. Our study thus reveals key principles for understanding histone methylation in proliferating, senescent, and differentiating cells. In contrast, H3K27 acetylation is regulated through a distinct, cell cycle-coupled mechanism. We find that CBP/Nejire-mediated acetylation of H3K27 peaks during S-phase and is reversed by HDAC1, as cells exit replication. Disruption of this acetylation cycle leads to replication stress and a G2 cell cycle arrest via a DNA damage checkpoint. Notably, this genome-protective function of CBP/Nejire depends specifically on acetylation of the H3K27 residue itself, revealing a novel role for H3K27ac beyond its well-established function in transcriptional activation. Together, our findings establish a robust link between cell cycle progression and histone modification dynamics, highlighting the necessity of maintaining balanced PTM levels under varying proliferative states. These insights have broad implications for our understanding of development, aging, and tumor growth.

INTRODUCTION

The cell cycle and the regulation of chromatin need to be tightly coordinated preserve epigenetic integrity. Specifically, progression through S-phase poses several challenges: chromatin must become transiently accessible for DNA replication, pre-existing post-translationally modified histones must be evenly distributed between daughter genomes and newly incorporated histones must acquire appropriate modifications to compensate for the semi-conservative dilution of modifications. These demands are complicated by the fact that cell cycle progression and dynamics differ drastically across biological contexts, ranging from rapid divisions in embryonic and regenerating tissues to complete arrest in terminally differentiated cells. How chromatin states are maintained across diverse proliferative tissue environments *in vivo* is still insufficiently understood.

In actively proliferating tissues, entry into the cell cycle at the G1/S transition, and progression through subsequent cycle phases, are tightly regulated. This regulation is mediated by Cyclins and Cyclin-dependent kinases (CDKs), as well as retinoblastoma (Rb) proteins and E2F transcription factors. Throughout the cell cycle, specific checkpoints respond to growth factors or cell size to modulate the rate of proliferation, as well as to DNA damage or chromosome misalignment to maintain the integrity of the genome (Matthews et al., 2022, Tapon et al., 2001, Lee and Orr-Weaver, 2003). As cells enter stages of differentiation, quiescence or senescence, they typically withdraw from active cycling by either prolonging their G1 phase or entering a stable cell cycle arrest known as G0. This transition away from proliferation often involves cyclin-dependent kinase (CDK) inhibitors, such as p21 and p27, which are intricately linked to gene expression programs that guide cell fate determination and differentiation (Buttitta and Edgar, 2007, Huang et al., 2022, de Morree and Rando, 2023, Ma et al., 2015). Progression through the cell cycle presents significant challenges for chromatin organization and epigenetic regulation - especially during S-phase but also during mitosis. Specifically, during S-phase, chromatin must become highly accessible to facilitate replication fork progression, nucleosome redistribution and de novo nucleosome incorporation in the replicated genomes (Stewart-Morgan et al., 2020, Alabert et al., 2015, Reveron-Gomez et al., 2018, Ma et al., 2015, Escobar et al., 2021, Ramos-Alonso and Chymkowitch, 2024). In contrast, in mitosis, chromatin must be tightly compacted to ensure accurate chromosome segregation (Ramos-Alonso and Chymkowitch, 2024, Zhou and Heald, 2020). Central to the regulation of chromatin organization are post-translational histone modifications (PTMs), which are also epigenetic regulators of transcriptional silencing and gene activation (Millan-Zambrano et al., 2022, Bhatnagar et al., 2023, Lopez-Hernandez et al., 2025). It is well-established that PTM dysregulation can lead to cell cycle defects by disrupting chromatin organization and entire gene regulatory networks (Brookes and Shi, 2014, Cavalli and Heard, 2019, Feinberg et al., 2016, Peterson and Laniel, 2004). While much attention has been dedicated to understanding how PTM dysregulation can drive pathogenesis by altering the expression of genes central to cell cycle regulation, less is known about how cell cycle dynamics connect to the maintenance and re-establishment of histone modifications. Yet, studies of the cell cycle-dependent regulation of the histone methyltransferase PR-Set7 and

87 histone demethylase PHF8 underscore the capacity of the cell cycle machinery to control specific
88 histone modifications and thereby maintain chromatin function (Oda et al., 2010, Liu et al., 2010).
89
90 Some of the most abundant PTMs that regulate chromatin accessibility and transcriptional activity are
91 acetylation and methylation of lysine residues on histone tails. While several lysine residues in histones
92 can be acetylated or methylated, research has most strongly focused on dynamic acetylation and
93 methylation of lysines 9 and 27 on histone H3 (H3K9 and H3K27), which represent some of the
94 functionally most important histone modifications. In most species, trimethylation of H3K27 is mediated
95 by Polycomb Repressive Complexes and relies on histone methyltransferases of the Enhancer of zeste
96 E(z) family. H3K27me3 maintains the silencing of many genes required for cell fate specification during
97 development, most famously Hox genes (Blackledge and Klose, 2021, Sparmann and van Lohuizen,
98 2006, Muller et al., 1995, Beuchle et al., 2001, Cao et al., 2002). In contrast, trimethylation of H3K9
99 (H3K9me3) is mediated by the enzymatic activity of Su(var)3-9 and is central to the formation and
100 maintenance of constitutive heterochromatin at telomeres, centromeres and repetitive repeats
101 (Padeken et al., 2022, Aagaard et al., 1999, Ebert et al., 2004). In *Drosophila*, H3K27 acetylation is
102 mediated by the histone acetyltransferase (HAT) Nejire (Nej), a homolog of mammalian p300/CBP, and
103 is reversed by the histone deacetylase HDAC1/Rpd3 (Willnow and Teleman, 2024, Petruk et al., 2001,
104 Tie et al., 2009, Ciabrelli et al., 2023). H3K27ac is strongly associated with active promoters and
105 enhancers, where it is thought to facilitate chromatin opening and transcriptional activation (Holmqvist
106 and Mannervik, 2013, Philip et al., 2015, Boija et al., 2017, McConnell et al., 2012, Chen et al., 2022).
107 As a consequence of these important functions, dysregulation of H3K9me3, H3K27me3 and H3K27ac
108 is a common feature in cancer or other diseases characterized by alterations and defects in cell
109 proliferation. Yet, importantly, it often remains unclear if defects in epigenetic modifications cause
110 altered proliferation defects or if vice versa proliferation defects cause defects in epigenetic
111 modifications (Brookes and Shi, 2014, Cavalli and Heard, 2019, Feinberg et al., 2016, Classen et al.,
112 2009). Disentangling this relationship is key to understanding how epigenetic and proliferative states
113 influence one another in development and disease.
114
115 Importantly, the semi-conservative nature of DNA replication during S-phase has a profound impact on
116 the landscape of these histone modifications. As the DNA is duplicated, pre-existing histones bearing
117 PTMs are equally distributed onto the newly synthesized strands. Naïve, newly synthesized histones
118 are integrated to ensure proper packaging of the duplicated genomes but also necessitating the
119 reestablishment of the now diluted PTM code (Escobar et al., 2021, Alabert and Groth, 2012, Escobar
120 et al., 2019, Wenger et al., 2023). To reestablish the epigenetic histone modification landscape after
121 incorporation of newly synthesized, naive histones, histone-modifying enzymes act post-replication by
122 using the modifications on old recycled histones as a template to modify the newly incorporated histones
123 (Stewart-Morgan et al., 2020, Annunziato, 2015, Flury and Groth, 2024). Importantly, in cultured cells,
124 histone acetylation marks are typically restored immediately after replication often via a transcription-
125 dependent process, while histone methylation is generally re-established during subsequent gap
126 phases (Alabert et al., 2015, Zee et al., 2012, Reveron-Gomez et al., 2018, Petruk et al., 2013).

Of note, strong acetylation of newly synthesized histones plays a specific cell-cycle-dependent role during S-phase. Hyperacetylation, for example at H4K5, H4K12, H3K14, H3K23 or H3K56, is observed during S-phase and facilitates recognition of newly synthesized histones by histone chaperone complexes, promoting their correct incorporation into newly synthesized chromatin. Hyperacetylation of histones presumably occurs in the cytoplasm and may be mediated by B-type acetyltransferases like Hat1 (Li et al., 2008, Masumoto et al., 2005, Tessarz and Kouzarides, 2014, Benson et al., 2006, Falbo and Shen, 2009, Jackson et al., 1976, Lande-Diner et al., 2009, Ruiz-Carrillo et al., 1975, Annunziato and Hansen, 2000, Sobel et al., 1995, Verreault et al., 1998).

Despite these insights, questions remain about how cell cycle progression influences histone modification dynamics, especially in *in vivo* settings. For instance, to what extent are histone modifications regulated in a cell cycle-dependent manner in developing tissues? How does the maintenance of these modifications differ between rapidly proliferating cells and cells in quiescent, senescent, or post-mitotic states? Moreover, how is the activity of histone-modifying enzymes coordinated with cell cycle checkpoints? To begin to address these questions we used the developing *Drosophila* wing imaginal disc to characterize cell cycle dependent histone modifications and reveal pronounced dynamics of H3K9 and H3K27 modifications in a developing tissue.

RESULTS

(1) Post-translational modifications of H3K27 and H3K9 are linked to cell cycle dynamics

To understand how cell cycle dynamics may affect chromatin dynamics, we aimed to identify post-translational histone modifications that are sensitive to changes in cell cycle progression. Using the *rn-GAL4* driver **(Fig S1.1A)**, under the control of a temperature-sensitive GAL80ts, we genetically manipulated cell cycle progression in the pouch of developing wing imaginal discs for 24 hours by accelerating or decelerating cell cycle dynamics. Within this timeframe of 24 h, we expect to disturb at least one cell cycle, which lasts between 12 and 18 h in third instar wing imaginal discs (Neufeld et al., 1998, Milan et al., 1996, Prober and Edgar, 2000, Crucianelli et al., 2022). First, we induced a cell cycle arrest in late G2 by expressing *Cdk1-RNAi (Cosolo et al., 2019)*. Second, ectopic expression of the ERK-responsive ETS transcription factor Pointed-P1 (PntP1) causes cells to arrest in either G1 or in G2 (Ito and Igaki, 2021). We confirmed the arrest in our genotypes by observing the cell cycle reporter FUCCI and the absence of EdU incorporation, a nucleotide analogue visualizing DNA replication, in nuclei of the *rn-GAL4* expression domain **(Fig S1.1B-L)** (Zielke et al., 2014). Conversely, we accelerated the cell cycle by co-expressing of dE2F1 and dDP (Buttitta et al., 2007, Neufeld et al., 1998). This did not alter the proportion of cells in G1 or G2 but resulted in elevated EdU incorporation, reflecting the accelerated S-phase dynamics - both in frequency and speed (Crucianelli et al., 2022) - of this genotype **(Fig S1.1M-Q)**.

167 As post-translational histone modifications are numerous, we focused on prominent modifications
168 mediated by well-known histone-modifying complexes. We analyzed modifications associated with
169 gene regulation, such as H3K27ac (mediated by the p300/CBP nejire), H3K9ac (mediated by SAGA-
170 HAT complex), H3K4me3 (mediated by the Trithorax (Trx)) and H3K27me3 (mediated by the Polycomb
171 protein E(z)), or modifications associated with genome maintenance, such as H3K9me3 (mediated by
172 Su(var)3-9), as well as examples of less well characterized modifications, such as H3K18ac and
173 H4K8ac (mediated by p300/CBP, Gcn5, SAGA-HAT), H3K18 crotonylation (mediated by the p300/CBP
174 nejire), and pan-H3K9 methylation or total lysine acetylation. We performed immunofluorescence
175 staining for these modifications in wing imaginal discs with the induced cell cycle alterations described
176 above.
177
178 Many of the histone modifications analyzed did not change upon manipulating cell cycle dynamics. For
179 example, H3K18ac and H3K4me3 levels were not sensitive to cell cycle modulation **(Fig 1A-D, I-L, U-**
180 **W, Fig S1.3A)**, and neither were H4K8ac, H3K9ac, H3K18 crotonylation, total H3K9 methylation nor
181 levels of total lysine acetylation **(Fig S1.2, Fig S1.3B)**. Yet, strikingly, we found that H3K27ac levels
182 were strongly reduced in cell cycle arrested genotypes, whereas levels of this modification were
183 elevated when the cell cycle was accelerated **(Fig 1E-H, U-W)**. In contrast, H3K9me3 and H3K27me3
184 levels were elevated in arrested cells, whereas levels of both modifications were reduced when the cell
185 cycle was accelerated **(Fig 1M-W)**. Importantly, alterations observed in cell cycle arrested cells were
186 independent of which cell cycle phase the arrest occurred in. Specifically, H3K27ac reduction and
187 H3K9me3 and H3K27me3 elevation was observed in both G1 and G2 arrested cell populations upon
188 expression of *pntP1* **(Fig S1.1I, Fig 1G,O,S)**, suggesting that the elongation of either gap phase can
189 produce the observed effects.
190
191 Taken together, we conclude that cell cycle dynamics have a surprising impact on histone modification
192 in a proliferating tissue. First, only three tested modifications responded significantly to cell cycle
193 dynamics in our assays, suggesting that only a subset of modifications is strongly linked to the cell cycle
194 machinery. Second, these changes were not dependent to cells arresting in G1 or in G2, suggesting
195 that overall cell cycle length is a defining factor rather than the gap phase position within a cell cycle.
196 Third, if levels of histone modifications were primarily determined by the kinetics of restoring histone
197 modifications after semi-conservative replication and the resulting histone PTM dilution, one may
198 predict that modifications simply accumulate as the cell cycle lengthens. However, the reduction of
199 H3K27ac in arrested cells defies a scenario in which continuous HAT activity restores H3K27ac levels
200 after DNA replication. We thus wanted to better understand the relationship between histone
201 methylation, histone acetylation and cell cycle dynamics.
202
203 **(2) Cell cycle dependent changes in H3K27ac, H3K27me3 or H3K9me3 levels occur at**
204 **preexisting target loci**
205

To first identify the genomic regions affected by the cell-cycle-dependent changes in bulk levels of H3K27ac, H3K27me3, and H3K9me3, we performed CUT&Tag analysis on wing imaginal discs expressing *Cdk1-RNAi* under the control of *rn-GAL4* for 24 hours. Although *Cdk1-RNAi* is expressed in only a subset of cells within the wing disc (see **Fig S1.1A**) - limiting the magnitude of detectable differences - we consistently observed a decrease in H3K27ac levels, and an increase in levels of both H3K27me3 and H3K9me3 modifications. These changes occurred at genomic regions already carrying these modifications in wild type conditions, as evident from examples of genomic snapshots **(Fig 2 A,B)** and changes in average levels of modification on and around peaks identified in both wild type and *Cdk1-RNAi*-expressing discs **(Fig 2 C-F, Fig S2.1A, E)**. These findings are consistent with prior observations in mESCs, where H3K27me3 levels increase at pre-existing sites during prolonged G1 phases (Trouth et al., 2025).

Of note, many H3K27ac peaks identified only in wild type samples exhibited a significant reduction in H3K27ac levels in *Cdk1-RNAi*-expressing discs, suggesting that H3K27ac was indeed lost from pre-existing acetylated regions **(Fig S2.1B,E)**. In agreement with this conclusion, genomic sequences not identified as peaks by our algorithm in any sample showed little or no change in H3K27ac levels **(Fig S2.1D, E)**. In contrast, although increases in H3K27me3 and H3K9me3 levels in *Cdk1-RNAi* discs occurred at many pre-existing methylated sites **(Fig S2.1A, E)**, a substantial number of H3K27me3 and H3K9me3 peaks identified only in *Cdk1-RNAi* discs, as well as sequences in other genomic regions, also showed significantly elevated methylation compared to wild-type controls **(Fig S2.1C,D,E)**. This indicates that the accumulation of H3K27me3 and H3K9me3 in *Cdk1-RNAi* discs may extend beyond canonical methylation target sites identified in wild type discs. We conclude that cell-cycle-dependent changes to bulk levels of H3K27ac, H3K27me3 or H3K9me3 predominantly affect existing target sites; however, the increase in methylation may also affect other genomic regions. Importantly, the magnitude of changes compared to levels of methylation in control discs is similar for all genomic regions, suggesting that changes to H3K27me3 or H3K9me3 levels occur at the same rate across the genome.

Our conclusions are further supported by our observations that the histone-modifying enzymes responsible for H3K27 acetylation and H3K27methylation do not compete for the same histone residues *in vivo*. Specifically, when we performed a knock-down of the H3K27 methyltransferase E(z), we observed an expected loss of H3K27me3 **(Fig S2.2 A,B)**, but importantly, no corresponding increase in H3K27ac **(Fig S2.2 C,D)**. Conversely, when we performed a knock-down of the H3K27 acetyltransferase CBP/Nej (Nejire), we observed an expected loss of H3K27ac **(Fig S2.2 E,F)**, but no corresponding increase in H3K27me3 **(Fig S2.2 G,H)**. We conclude that, even though studies propose local antagonism of H3K27me3 and H3K27ac at the same residues (Tie et al., 2016, Philip et al., 2015, Tie et al., 2009), the cell-cycle-length-dependent decrease of H3K27ac and increase of H3K27me3 bulk levels upon expression of *Cdk1-RNAi* are not driven by competition for the same H3K27 residues but instead reflect their natural occurrence of these distinct PTMs in distinct genomic contexts.

(3) H3K27 or H3K9 modifications are linked to cell cycle dynamics during development

If bulk histone modifications in wing discs are affected by cell cycle progression, can we provide evidence that this also occurs in a physiologically relevant state? During larval development, cells in the wing imaginal disc actively proliferate. However, the future wing margin forms a zone of non-proliferating cells (ZNC), where cells arrest in either G1 or G2 **(Fig S3.1 A-C)** (Johnston and Edgar, 1998). In addition to the ZNC, two clusters of G2-arrested cells with senescent markers can be found surrounding the wing pouch **(Fig S3.1 D)** (Zang et al., 2025). Strikingly, arrested cells in the ZNC **(Fig 3 A-C)** and senescent clusters **(Fig 3 D-F)** show a decrease in H3K27ac levels and an increase in H3K9me3 and H3K27me3, consistent with our previous conclusions upon cell cycle elongation by expression of *Cdk1-RNAi* or *UAS-pntP1.* Importantly, none of the other histone modifications recapitulated this pattern, again reinforcing the specific association between H3K9me3, H3K27me3 and H3K27ac levels and the dynamics of cell cycle progression **(Fig S3.1 E-H)**.

To begin to understand if there are consequences for cell-cycle-dependent PTM modulation during development, we analyzed, as an example of three PTMs, H3K27me3-dependent regulation of cell fates. H3K27me3 mediates Polycomb-dependent silencing of genes typically required for cell fate specification (Blackledge and Klose, 2021, Sparmann and van Lohuizen, 2006, Beuchle et al., 2001). In imaginal disc with either arrested (*Cdk1-RNAi*) or accelerated (*Dp,E2F1*) cell cycle dynamics, the expression of Polycomb targeted genes required for wing disc differentiation, such as Antp, Ubx/AbdA, En/inv, Nub, Wg, Ptc and Cut was not altered **(Fig S3.2)**. These observations demonstrate that reduced or elevated H3K27me3 levels observed upon changing cell cycle dynamics still ensure robust Polycomb target gene outputs, suggesting that a H3K27me3 levels buffer gene silencing against a range of cell cycle dynamics.

Surprisingly, our subsequent experiments revealed that the cell cycle-dependent regulation of H3K9me3, H3K27me3, and H3K27ac arises through mechanistically distinct pathways. Specifically, methylation and acetylation marks exhibit fundamentally different dynamics. Given these divergent mechanisms, we present our findings in two consecutive sections: first, we detail how H3K9me3 and H3K27me3 levels are coupled to the cell cycle via growth signaling pathways **(Fig. 4)**, followed by an independent analysis of the function of H3K27ac in preventing replication stress during S-phase **(Figs. 5 and 6)**.

(4) H3K27me3 or H3K9me3 are coupled to cell cycle dynamics via metabolic signaling

Previous studies suggest that H3K27me3 and H3K9me3 modifications after DNA-replication are reestablished after DNA replication through slow and continuous methyltransferase activity in subsequent gap phases (Alabert et al., 2015, Zee et al., 2012, Reveron-Gomez et al., 2018). Our findings are consistent with these observations: in all our imaginal disc models, levels of H3K9me3 and H3K27me3 increase in conditions with elongated cell cycles (and thus infrequent S-phase events, reducing replication-associated dilution of these marks), and decrease in conditions with shortened cell

286 cycles (increasing the frequency of S-phase and thereby enhancing dilution). These results suggest
287 that H3K9 and H3K27 methylation is driven by a relatively constant rate of histone methyltransferase
288 activity, which appears not to be affected by genetic alterations of the cell cycle machinery. If the rate
289 of histone methylation can indeed be genetically separated from the frequency of cell cycling, what
290 mechanisms then govern the restoration of histone methylation to the appropriate levels, particularly for
291 H3K9me3, which is essential for heterochromatin architecture, and H3K27me3, which is critical for gene
292 silencing? To address this question, we decided to manipulate cell cycle progression upstream of direct
293 regulators of the cell cycle by activating a proliferative pathway with important metabolic functions.
294 Specifically, we expressed a constitutively active Insulin receptor (InR^{DA}) under the control of *rn-GAL4*
295 for 24 h, which promotes PI3K/Akt signaling. The resulting metabolic changes can be visualized by
296 higher rates of protein synthesis reflecting higher biosynthetic capacity, accelerated cell proliferation
297 visualized by high EdU incorporation and ultimately, larger wing pouch size **(Fig 4A-C, Fig S4 A-E)**. Of
298 note, expression of InR^{DA} did not alter the FUCCI cell cycle profile, demonstrating that the higher
299 metabolic activity shortens the overall cell cycle length, rather than affecting specific cell cycle phases
300 **(Fig S4F,G)**.
301
302 Importantly, we found that expression of InR^{DA} alone did not give rise to changes in H3K27 or H3K9
303 methylation levels, despite the accelerated cell divisions **(Fig 4 D,E,H, I)**. This demonstrates that the
304 metabolic potential can tune the rate of H3K27 and H3K9 methylation, to keep levels of H3K27 or H3K9
305 methylation comparable to wild type levels, despite accelerated cell cycle progression. To now
306 functionally separate metabolic potential from cell cycle progression, we also arrested the cell cycle by
307 co-expressing the constitutively active Insulin receptor with a *Cdk1-RNAi*. As expected from our
308 previous experiments, levels of H3K27me3 and H3K9me3 increased, but most strikingly, levels of
309 H3K27me3 and H3K9me3 were even higher than in discs expressing *Cdk-1-RNAi* alone **(Fig 4F,G,J,K)**.
310 These results demonstrate that rates of H3K27 or H3K9 methylation are intimately linked to the
311 metabolic potential of a cell - with the purpose to match the rate of H3K27 or H3K9me3 methylation
312 with the speed of cell cycle progression and thus the frequency of S-phase linked histone dilution **(Fig
313 4 P,Q)**. Of note, levels of H3K4me3 were not affected by these manipulations **(Fig 4 L-O)**, indicating
314 that a modification maintaining steady levels of bulk transcriptional activity is not - and even should not
315 be - linked to metabolic rates or the rate of cell cycle progression.
316
317 We wanted to better understand the functional implications of our findings. The link between levels of
318 H3K9me3 and cell cycle progression becomes relevant in physiological and pathological setting of
319 senescence, where cytotoxic stress or oncogenic mutations provide metabolic activation that is
320 juxtaposed to a senescent cell cycle arrest program. Accordingly, in senescent G2-arrested cells at the
321 center of inflammatory tissue damage in wing imaginal discs induced by ectopic expression of the TNFα
322 homologue eiger (egr) **(Fig S4.2 A-F)** (Cosolo et al., 2019, Floc'hlay et al., 2023, Jaiswal et al., 2023,
323 Smith-Bolton et al., 2009), we observed high levels of H3K9 methylation **(Fig S4.2G-I, purple)**.
324 Importantly, levels in senescent cells with inflammatory metabolism were higher than in quiescent cells
325 at the disc periphery, which exhibit low insulin-signaling activity **(Fig S4.2G-I, yellow)** (Maya et al.,

326 2024). These observations support our conclusions that high and low metabolic activity coupled to cell
327 cycle arrest produce different levels of H3K9me3. We thus propose that the widely reported
328 senescence-associated heterochromatinization associated with elevated H3K9me3 during oncogene-
329 induced senescence may not be a feature of the senescence program *per se* but rather a consequence
330 of continuous H3K9 trimethylation driven by metabolic activation from oncogenic mutations in the
331 absence of cell division (Hernandez-Segura et al., 2018, Huang et al., 2022, Narita et al., 2003). Finally,
332 in agreement with our previous conclusions, we found that cells undergoing fast regenerative
333 proliferation around the site of inflammatory damage have lowest levels of H3K9me3 **(Fig S4.2G-I,**
334 **cyan)**.
335
336 **(5) CBP/nejire-mediated H3K27 acetylation is high during S-phase**
337
338 Having revealed how H3K9me3 and H3K27me3 dynamics are coupled via metabolic cues to the cell
339 cycle, we now wanted to characterize the observed cell cycle dynamics of H3K27 acetylation. The
340 downregulation of H3K27ac by cell cycle elongation and the upregulation of H3K27ac by cell cycle
341 acceleration contradicts the simple explanation that an enzymatic activity acetylates H3K27 at a
342 constant rate. To better understand H3K27ac dynamics, we performed a detailed analysis of H3K27ac
343 levels throughout the cell cycle by correlating H3K27ac with FUCCI reporters in wing imaginal discs.
344 We specifically excluded mitotic cells from this analysis, as the highly condensed nature of their
345 chromosomes and the cells' extreme apical position prevented a direct comparison to other cell cycle
346 stages.
347
348 Using this approach, we found that H3K27ac levels were significantly increased in nuclei of early and
349 late S-phase cells if compared to G1 and G2 phases **(Fig 5A-C)**. This increase, and especially the
350 much higher levels in late S-phase in comparison to G2, could only partially be recapitulated by changes
351 in total H3 or total acetyl-Lysine levels **(Fig S5.1 A-F)**. Of note, fluctuation of H3 and total lysine
352 acetylation in our microscopy assays can be mostly explained by S-phase dependent histone synthesis
353 and histone acetylation, as well as fluctuating morphology of interphase nuclei (Stein et al., 1975,
354 Mendiratta et al., 2019, Verreault et al., 1998). Our finding that H3K27ac levels are higher throughout
355 S-phase are consistent with our earlier observations: cells which cycle fast repeatedly enter S-phase
356 and cells which cycle slowly are not often found in S-phase, hence bulk H3K27ac levels in a proliferating
357 and arrested tissue will appear high and low, respectively.
358
359 These results suggest that the enzymes responsible to regulate H3K27 acetylation may exhibit cell-
360 cycle-dependent regulation. Knock-down of the H3K27ac HAT CBP/nej via RNAi (*neijire-RNAi*)
361 expressed for 24 h under the control *rn-GAL4*, completely abolished H3K27ac staining in the wing
362 pouch, confirming that CBP/nej is the main source of H3K27 acetylation in the wing disc **(Fig 5 D-E)**
363 (Willnow and Teleman, 2024). To provide specific proof that CBP/nej mediates S-phase-dependent
364 H3K27 acetylation, we overexpressed CBP/nej for 24 h under the control of *rn-GAL4* and correlated
365 H3K27ac levels with cell-cycle phases using the FUCCI reporter. While global H3K27ac increased upon

366 CBP/nej overexpression **(Fig 5F,G,J; Fig S5.1 G,H)**, we observed a disproportionate increase of
367 H3K27ac in late S-phase cells **(Fig 5J')**. This demonstrates that CBP/nej-driven acetylation of H3K27
368 is especially pronounced during S-phase and indicates that H3K27ac accumulates ectopically in late
369 S-phase cells when CBP/nej levels are too high. In support of a model where CBP/nej is specifically
370 active during S-phase, we found that levels of two other CBP/nej-mediated modification (H3K18ac and
371 H4K8ac) showed a less pronounced but still detectable increase in S-phase cells of normally
372 proliferating wild type tissue **(Fig S5.2 A-F)**, which is consistent with the reduced CBP/nej substrate
373 specificity for these two residues, as well as for H3K18 crotonylation, observed in CBP/nej-RNAi
374 experiments **(Fig S5.2 G-N)**.
375
376 As these targeted overexpression experiments suggested that CBP/nej levels may influence S-phase-
377 dependent activity, we examined a CBP/nej-GFP fusion protein expressed from the endogenous locus
378 to assess if CBP levels fluctuate during the cell cycle (Marsh et al., 2025). We found that, in proliferating
379 wing discs, nuclear GFP levels were mostly uniform in all cells **(Fig S5.2 O)**, indicating that regulation
380 of CBP/nej enzymatic activity, rather than cell cycle dependent changes in protein levels, underlies the
381 S-phase-specific activity. Indeed, in cultured cells, CBP/p300 activity may be regulated by cyclin-
382 dependent kinases at the G1/S transition (Ait-Si-Ali et al., 1998).
383
384 The pronounced reduction of H3K27ac in late-S-phase, and subsequently in G2-phase or G1-phase
385 cells, which we observed in development, in arrested cell populations and upon CBP/nej overexpression
386 or knock-down, demonstrates that the removal of H3K27ac in late S-phase must be a highly controlled
387 process. Removal of acetylation from the H3K27 residue would likely be mediated by HDAC activity.
388 We thus depleted the primary H3K27 deacetylase HDAC1 (Rpd3) via expression of an RNAi construct
389 under the control of *rn-GAL4* for 24 h (Willnow and Teleman, 2024). HDAC1 knockdown led to a mild
390 but detectable overall increase in H3K27ac, consistent with its role in H3K27ac removal **(Fig 5 H, I, K;**
391 **Fig S5.1 I,J)**. Yet, importantly, we observed a disproportionate increase of H3K27ac in late S-phase
392 cells, supporting a model where HDAC1 is required to specifically remove H3K27ac in late S-phase
393 **(Fig 5K')**.
394
395 **(6) CBP/nej activity and H3K27acetylation is required to prevent replication stress during S-**
396 **phase**
397
398 We finally wanted to understand what function elevated CBP/nej activity during S-phase may serve. To
399 analyze if elevated CBP/nej activity may reflect a specific requirement during DNA replication, we
400 conducted a knock-down of *CBP/nej* in the wing pouch under the control of *rn-GAL4* for 24 h. We first
401 analyzed DNA replication by EdU incorporation and found a wide-spread decrease in the number of
402 cells entering S-phase and in DNA replication activity, suggesting that both S-phase entry and
403 progression was severely slowed within 24 h of *CBP/nej* knock-down **(Fig 6A-C)**. To determine if DNA
404 replication during *CBP/nej* knock-down had proceeded successfully, we investigated if *CBP/nej-RNAi*-
405 expressing cell experienced replication stress. We thus analyzed levels of phosphorylated γH2A, a

marker of DNA double strand breaks which can arise at stalled replication forks (Madigan et al., 2002, Petermann et al., 2010). In all wild type tissues, we observed a similar number of high intensity nuclei positive for γH2A, likely representing physiological cell death or (unspecific) binding of the antibody in mitotically active cells (Khan et al., 2017). However, the majority of nuclei are negative for γH2A **(Fig 6D,F)**. Strikingly, in all nuclei of *CBP/nej-RNAi* -expressing cells, we observed a pronounced increase in nuclear γH2A levels - which were represented by medium fluorescence intensities. The γH2A signal covered the entire nuclei, suggesting wide-spread DNA damage **(Fig 6E,G,H)**. We conclude that CBP/nej is specifically required to prevent genome-wide replication stress during S-phase. Accordingly, *CBP/nej-RNAi*-expressing cells cannot progress through the cell cycle and completely arrest in G2 **(Fig 6I,J)**. In tissue damage models of wing discs, cells arrest in G2 as a consequence of stress-dependent activation of JNK-signaling, which downregulates *cdc2/stg* (Cosolo et al., 2019). Yet, co-expressing a dominant-negative JNKK (bskDN) in *CBP/nej-RNAi*-expressing caused pronounced downregulation of JNK activation **(Fig S6A-C)**, but still resulted in G2 arrested cells **(Fig S6D)**. This strongly indicates that a very specific function of CBP/nej in DNA replication caused a G2 cell cycle arrest by activation of a DNA damage checkpoint, rather than the non-specific activation of cellular stress signaling through JNK. These observations are thus consistent with a model were high levels of CBP/nej-mediated H3K27ac are specifically required to ensure faithful DNA replication and to prevent DNA damage and consequently, a DNA damage induced cell cycle arrest in G2. Of note, analysis of *CBP/nej*-overexpressing tissues revealed normal patterns of EdU incorporation and distribution, suggesting that cells with high - but still cell-cycle-dependent - levels of H3K27ac proliferate normally **(Fig S6E-G)**.

CBP/nej targets a wide range of substrates, including several non-histone proteins (Stauffer et al., 2007, Cazzalini et al., 2014, Dutto et al., 2018, Tillhon et al., 2012, Ramadan et al., 2025, Ogiwara et al., 2011). We thus wanted to determine, if the function of CBP/nej in preventing replication stress is mediated by its substrate H3K27. Especially, since H3K27 was the histone substrate most sensitive to the loss of CBP/nej activity in our assays **(**refer to **Fig S5.2 G-N)**. To test this, we generated mosaic clones homozygous for a deletion of the entire histone gene cluster (ΔHisC), whose viability was rescued by 12 copies of a histone gene unit in which wild type H3 was replaced with a non-modifiable H3K27R amino acid substitution (Pengelly et al., 2013). As previously reported, these clones lose Polycomb gene silencing function normally mediated by H3K27me3, and exhibit derepression of Hox genes such as *AbdB* **(Fig S6H,I)** (Pengelly et al., 2013). When we assessed if these cells also exhibit replication stress, we observed broad and elevated levels of γH2A in the H3K27R-substituted clones **(Fig 6K)**. These findings suggest that the function of CBP/nej in mitigating replication stress during DNA replication may be, at least in part, mediated through its modification of H3K27 **(Fig 6I)**.

DISCUSSION

Our work dissects the link between H3K27ac, H3K27me3, and H3K9me3 modification dynamics and dynamics of the cell cycle in proliferating tissues *in vivo*. We demonstrate that both physiological and genetically induced elongation of the cell cycle leads to elevated bulk levels of H3K27me3 and

446 H3K9me3. Conversely, accelerated cell cycle progression specifically decreases these histone
447 marks. Genome-wide analyses using CUT&tag assays revealed that these changes occur
448 predominantly at their distinct pre-existing genomic target loci, implicating canonical histone readers
449 and modifiers in mediating these cell cycle-dependent changes. Importantly, despite cell cycle-
450 dependent changes in bulk H3K27me3 levels, expression patterns of Polycomb target genes remained
451 unaffected, implying that H3K27me3-dependent gene silencing at target loci is buffered even under
452 altered cell cycle conditions. Mechanistically, we found a tight coupling between histone methylation
453 rates and cell division frequency, mediated by cellular metabolic activity. Specifically, H3K27me3 and
454 H3K9me3 levels remained normal upon expression of a constitutively active Insulin receptor,
455 suggesting that cells channeled the higher metabolic activity into accelerated cell divisions and
456 maintained H3K27me3 and H3K9me3 levels proportional to cell division rates. Remarkably, active
457 Insulin receptor-expressing cells forced to arrest their cell cycle accumulated levels of H3K27me3 and
458 H3K9me3 to much higher levels than arrested wild type cells, demonstrating that metabolic rate tunes
459 the rate of histone methylation to match the frequency of S-phase occurrence, i.e. the frequency of cell
460 divisions. These observations have important implications for chromatin dysregulation in pathological
461 conditions, such as cancer, where the tight coordination between metabolic and cell cycle rates
462 becomes compromised. An important implication of our findings relates to the emergence senescence-
463 associated heterochromatin, a phenomenon well-documented during oncogene-induced senescence
464 (Hernandez-Segura et al., 2018, Huang et al., 2022, Narita et al., 2003). Our data suggest that
465 H3K9me3 accumulation in senescence-associated heterochromatin may reflect persistent
466 methyltransferase activity driven by aberrant metabolic stimuli in the absence of replication-dependent
467 dilution. Thus, the observed chromatin state in senescent cells may be a consequence of the mismatch
468 between metabolic and cycling rate, rather than an intrinsic feature of the senescence phenotype itself.
469 An important implication of our findings is that post-mitotic and differentiating cells, such as neurons,
470 must tightly regulate histone-modifying activities to prevent the aberrant accumulation of repressive
471 marks, such as H3K9me3 and H3K27me3.
472
473 Furthermore, we observed that H3K27ac exhibits a unique, cell cycle–dependent profile, peaking
474 significantly during S-phase. While hyperacetylation of newly synthesized histones at various residues
475 during S-phase is well-established, an S-phase dependent increase in nuclear acetylation of H3K27
476 has not been reported (Li et al., 2008, Masumoto et al., 2005, Tessarz and Kouzarides, 2014, Benson
477 et al., 2006, Falbo and Shen, 2009, Jackson et al., 1976, Lande-Diner et al., 2009, Ruiz-Carrillo et al.,
478 1975, Annunziato and Hansen, 2000, Sobel et al., 1995). We propose this peak in acetylation during
479 S-phase is mediated by CBP/nej, potentially regulated by cyclin-dependent kinases at the G1/S
480 transition (Ait-Si-Ali et al., 1998). Correspondingly, our data is consistent with the idea that H3K27
481 becomes deacetylated during late S-phase by HDAC1. Generally, HDAC activity is reported to remove
482 hyperacetylation on newly synthesized histone at the end of S-phase to reestablish higher order
483 chromatin organization (Annunziato and Seale, 1983). However, whether the H3K27 acetylation cycle
484 mediated by CBP and HDAC 1 occurs on old histones, newly synthesized histones, or on newly

incorporated histones cannot be resolved with our methods. Yet, the observed H3K27 acetylation cycle reveals novel cell cycle dependent targets of CBP/nej and HDAC1.

Functionally, we demonstrate that CBP/nej activity is essential during S-phase to prevent DNA damage from replication stress and consequently delays in cell cycle progression mediated by a replication checkpoint. In fact, previous studies find that CBP/nej and ATR mei-41 are required for the replication checkpoint itself to function properly (Smolik and Jones, 2007, Stauffer et al., 2007). This may be explained by acetylation non-histone substrates by CBP/p300, which stabilizes key DNA damage repair factors, including PCNA, ATR and ATM, thereby facilitating DNA repair following damage (Stauffer et al., 2007, Cazzalini et al., 2014, Dutto et al., 2018, Tillhon et al., 2012, Ramadan et al., 2025, Ogiwara et al., 2011). Consistent with this, mutations in EP300 result in persistent replication stress, replication fork collapse, genomic instability, and embryonic proliferation defects (Barreto-Galvez et al., 2023; Yao et al., 1998). (Barreto-Galvez et al., 2023, Yao et al., 1998). Collectively, these findings underscore the essential role of CBP/p300-mediated acetylation in regulating replication integrity and genomic stability beyond traditional cell cycle regulation. Importantly, our findings extend this previous work by providing mechanistic insight, indicating that *in vivo* this function is mediated by acetylation of H3K27, a target commonly regulated by CBP/nej and HDAC1. Notably, cells carrying the H3K27R mutation exhibit derepression of Hox genes, closely resembling the phenotype associated with loss-of-function mutations in PRC1 and PRC2 complexes(Pengelly et al., 2013, Classen et al., 2009, Beuchle et al., 2001). However, H3K27R cells also display a pronounced, albeit not complete, reduction in overall H3K27ac levels – in contrast to the nearly complete loss of H3K27ac observed after 24 h of CBP/nej RNAi-expression. This suggests that CBP/nej-mediated acetylation of K27 may occur on both H3 and H3.3 variants, with the anti-H3K27ac antibody likely recognizing both forms and the broad substrate specificity of CBP/nej likely targeting both histone variants. Importantly, acetylation of H3 and H3.3 at K27 may carry distinct functional implications. H3.3 variants appear to be particularly critical for enhancer-associated H3K27ac thereby serving roles in interphase cells (Trovato et al., 2020), whereas acetylation of canonical H3 may regulate chromatin function and DNA replication in S-phase. Indeed, associations of H3K27ac with Origin Recognition Complex-binding sites and its requirement for gene amplification during endoreplication (Aggarwal and Calvi, 2004, Eaton et al., 2011, Hua and Orr-Weaver, 2017, McConnell et al., 2012), suggests that elevated levels of H3K27ac may be essential to establish an open chromatin environment necessary for efficient DNA replication. Collectively, these findings position H3K27ac as a central regulator integrating chromatin structure, DNA replication and genome integrity.

In conclusion, our findings establish a robust mechanistic link between cell cycle dynamics, metabolic signaling and histone modification of H3K27 and H3K9, and specifically implicate H3K27ac as critical mediator of replication fidelity and chromatin organization. These insights highlight the necessity of maintaining balanced histone modification levels to preserve genomic stability, particularly under varying proliferative and metabolic states, with broad implications for developmental biology, aging, and cancer biology.

526 **EXPERIMENTAL PROCEDURES**

527

528 ***Drosophila* genetics**

529 All experiments were performed on *Drosophila melanogaster*. Fly strains (see Table S1) were
530 maintained on standard fly food (10L water, 74,5g agar, 243g dry yeast, 580g corn flour, 552ml
531 molasses, 20.7g Nipagin, 35ml propionic acid) at 18°C – 22°C. Larvae from experimental crosses were
532 allowed to be fed on Bloomington formulation (175.7g Nutry-Fly,1100ml water 20g dry yeast, 1.45g
533 Nipagin in 15ml Ethanol, 4.8ml Propionic acid) and raised at 18°C or 30°C to control GAL80ts-
534 dependent induction of GAL4/UAS. To drive expression of UAS-constructs, such as *UAS-Cdk1-RNAi*,
535 under the control of *rn-GAL4* in the wing pouch, experiments were conducted following protocols from
536 Smith-Bolton et al. (2009), La Fortezza et al. (2016), and Cosolo et al. (2019), with slight modifications.
537 Briefly, larvae with the genotype *rn-GAL4, tub-GAL80^{ts}* and appropriate UAS-transgenes were staged
538 by a 6 hours egg collection and raised at 18°C with a density of 50 larvae per vial. Transgene expression
539 was activated by shifting the temperature to 30°C for 24 hours on day 7 after egg deposition (AED).
540 Unless otherwise noted, dissections were performed immediately after this induction period (recovery
541 time point R0). Control genotypes were derived from either rn^{ts} control crosses or sibling animals
542 (+/TM6c). All experiments were performed with at least ≥ 2 independent experimental replicates. Our
543 experimental design did not consider differences between sexes unless for genetic crossing schemes.

544

545 **FLP/FRT-Mediated Clone Induction**

546 Mitotic recombination to generate mosaic clones of the *Drosophila* histone gene cluster (ΔHisC) was
547 induced using the FLP/FRT system. Adult flies were allowed to lay eggs for 72 hours at 25 °C. FLP
548 recombinase expression was triggered by a 1-hour heat shock at 37 °C. Larvae were dissected either
549 48 or 72 hours after heat shock for subsequent analysis. Transgene cassettes providing a total of 12
550 copies of the Histone gene unit with a H3K27R point mutation (12×His-GUH3-K27R) rescues cell
551 viability of (ΔHisC) mutant clones (see (Pengelly et al., 2013)).

552

553 **Immunohistochemistry of wing imaginal discs**

554 To visualize histone modifications, wing discs from third instar larvae were dissected and fixed for 10
555 minutes at room temperature in 4% paraformaldehyde in PBS. Washes were performed in PBS
556 containing 0.1% TritonX-100 (PBT). The discs were then incubated with primary antibodies (**Table S1**)
557 in 0.1% PBT, gently mixing 2-overnights at 4°C. During incubation with cross-absorbed secondary
558 antibodies coupled to Alexa Fluorophores (Table S1) at 4°C for 1-overnight, tissues were
559 counterstained with DAPI (0.25 ng/µL, Sigma, D9542). Tissues were mounted using SlowFade Gold
560 Antifade (Invitrogen, S36936). To visualize DNA damage using the anti-H2AvD phosphoS137 antibody,
561 wing discs were fixed 5 minutes at room temperature in 4% paraformaldehyde in PBS. Washes were
562 performed in PBS containing 0.5% TritonX-100. The primary antibody was incubated in 0.5% PBT
563 overnight at 4°C and the secondary antibody in 0.5% PBT for 2 hours at room temperature. For all other
564 staining protocols, discs were fixed for 15 minutes at room temperature in 4% paraformaldehyde in
565 PBS. All washes and incubations were performed in PBS containing 0.1% TritonX-100 as described

566 above.To maintain consistency in staining across genotypes, control and experimental wing discs were
567 processed together in the same vial throughout the protocol and mounted on the same slide whenever
568 possible. Images were acquired using the Leica TCS SP8 Microscope, using the same confocal settings
569 for linked samples and processed using tools in Fiji. Figure panels were assembled in Affinity Designer
570 2.
571
572 **EdU labelling**
573 EdU incorporation was performed using the Click-iT Plus EdU Alexa Fluor 647 Imaging Kit (Table S1).
574 Briefly, larval cuticles were inverted in Schneider's medium and incubated with EdU (10μM final
575 concentration) at RT for 15 minutes. Cuticles were then fixed in 4% PFA/PBS for 15 minutes, washed
576 for 30 minutes in PBT 0.5%. EdU-Click-iT labeling was performed according to manufacturer's
577 guidelines. Tissues were washed in PBT 0.1%, after which immunohistochemistry, sample processing
578 and imaging were carried out as described above.
579
580 **SA-β-Gal staining**
581 CellEvent senescence detection kit from Invitrogen (Table S1) was used to check senescence-
582 associated β-galactosidase activity, following the manufacturer instructions. Briefly, larvae were
583 dissected in PBS, fixed with 4% PFA, washed with 1% BSA (in PBS), and then incubated in working
584 solution for 2h at 37°C. Washing steps were performed in PBS and PBS containing 0.1% TritonX-100
585 (PBT). Tissues were counterstained with DAPI (0.25 ng/μl). Further immunohistochemistry analysis and
586 sample mounting was performed as described above.
587
588 **Protein synthesis assay using OPP- Click-iT staining**
589 OPP Assays were performed using Click-iT® Plus OPP Protein Synthesis Assay Kits (Invitrogen
590 Molecular Probe) according to manufacturer's instructions. Briefly, larvae were dissected and inverted
591 cuticles were incubated with a 1:1000 dilution of Component A in Schneider's medium for 15 minutes
592 on a nutator. Larval cuticles were fixed with 4% paraformaldehyde for 15 minutes, rinsed twice in 0.1%
593 PBT, and permeabilized with 0.5% PBT for 15 minutes. The cuticles were then stained with the Click-
594 iT® cocktail for 30 minutes at room temperature, protected from light. Further immunohistochemistry
595 analysis and sample mounting was performed as described above.
596
597 **CUT&Tag sample preparation**
598 Briefly, for each genotype around 80-100 wing discs were dissected in ice cold Schneider's medium,
599 collected, snap frozen and stored at -80°C until further use. Nuclei were isolated with the help of a
600 mechanical pestle and processed for CUT&Tag analysis as previously described (Zenk et al., 2023,
601 Cardamone et al., 2025). For normalizing the levels of histone H3 modifications and as a proxy of the
602 starting material in each condition, we also generated samples for total histone H3. Libraries were
603 prepared by supplementing the NEBNext HighFidelity 2× PCR Master Mix with 1 pg of Tn5-tagmented
604 lambda DNA (New England Biolabs, #N3011S) as a spike-in normalizer. The library indexing was
605 performed using Illumina i5 and i7 (Buenrostro et al., 2015) through 15 cycles (1 x 5 min at 72 °C, 1 x

606 30 sec at 98°C, 13 x 10 s at 98 °C, 30 sec at 63 °C, 1 x 1 min at 72 °C, hold at 4 °C). The libraries were
607 purified using Nucleomag NGS Clean-up and Size Select beads (Macherey-Nagel, #744970.50).
608 Quality checks were done with Qbit DNA HS Assay (ThermoScientific, #Q32854) and Bioanalyzer
609 (Agilent). Finally, two independent library replicates were sent for next generation sequencing.
610
611 **QUANTIFICATIONS, BIOINFORMATIC ANALYSIS AND STATISTICS**
612
613 **General comments**
614 For all quantifications of imaging data, control and experimental samples were processed together and
615 imaged in parallel, using the same confocal settings. Images were processed, analyzed and quantified
616 using tools in Fiji (ImageJ 2.9.0) (Schindelin et al., 2012). Extreme care was taken to apply consistent
617 methods (i.e., number of projected sections, thresholding methods, processing) for image analysis.
618 Figure panels were assembled using Affinity Designer 2.6.2. Statistical analyses were performed in
619 Graphpad Prism. Illustrations were created in Biorender.
620
621 **Quantification of histone modifications**
622 For quantification of levels of histone modifications, an xy-representation containing the maximum
623 number of pouch and hinge cells was generated using a sum projection of the relevant channel. Three
624 square regions of interest (ROIs) measuring 15 × 15 µm were placed in distinct areas of either the
625 pouch or the hinge, carefully excluding regions with developmentally arrested cells. The mean intensity
626 of the modification signal was measured within each ROI. For each disc, the average pouch signal was
627 normalized to the average hinge signal and reported as a pouch-to-hinge intensity ratio.
628
629 **Quantification of EdU incorporation**
630 Figure S1.1: To first create a nuclear mask, an xy- representation containing the maximum number of
631 pouch nuclei was generated using a sum projection of the DAPI channel. The background signal was
632 reduced using the "Subtract Background" function with a rolling ball radius of 100 pixels. Local contrast
633 was enhanced with the "Enhance Local Contrast (CLAHE)" function, using a block size of 127, 256
634 histogram bins, and a maximum slope of 3. Automatic thresholding was performed using the "Moments"
635 method with the "dark" option selected, and the image was then converted into a binary mask of DAPI-
636 positive nuclear areas. A nuclear ROI was generated from this mask using the selection tool. The pouch
637 region was manually selected based on wing fold morphology. To isolate the nuclei within the pouch, a
638 binary "AND" operation was used to combine nuclear mask and pouch selection. This final pouch-
639 specific DAPI mask was used to measure EdU signal intensity.
640 Figure 6: To create an EdU mask, an xy- representation containing the maximum number of pouch
641 nuclei was generated using a sum projection of the EdU channel. A "Gaussian blur" (σ = 2) was applied
642 to reduce noise and smooth the signal. Automatic thresholding was then performed using the
643 "Moments" method with the "dark" option selected. The image was converted into a binary EdU mask
644 with a black background. A ROI was generated from this mask using the selection tool to define EdU-
645 positive pixels. Separately, the pouch region was manually selected based on wing fold morphology.

646 To isolate EdU-positive pixels specifically within the pouch, a binary “AND” operation was applied to
647 combine the EdU selection with the pouch selection. This final pouch-specific EdU mask was used to
648 measure EdU signal intensity.
649 To assess changes in the number of proliferating cells, pouch-specific DAPI and EdU masks were
650 generated as described above. A binary “AND” operation was used to extract EdU-positive nuclei
651 located within DAPI-positive regions in the pouch. The area of EdU-positive nuclei was then divided by
652 the total area of EdU and DAPI-positive regions within the pouch to calculate the fraction of proliferating
653 cells. This EdU-to-DAPI area ratio was calculated per disc and used for comparative analysis.
654
655 **Quantification of OPP levels in wing imaginal discs**
656 An xy-representation containing the maximum number of pouch cells was generated using a sum
657 projection of the relevant channels. In both control and constitutively active insulin receptor-expressing
658 discs, the pouch region was manually selected based on wing fold morphology. Mean OPP intensity
659 was then measured within the defined pouch region for each disc.
660
661 **Quantification of pouch size**
662 For both control and constitutively active insulin receptor-expressing discs, a slice containing the
663 maximum number of pouch cells was selected. In each case, the pouch region was manually defined
664 based on wing fold morphology. The area size of the selected pouch region was then measured for
665 each disc.
666
667 **Cell cycle phase classification using FUCCI and quantifications of H3, Total Acetyl Lysine,**
668 **H3K27ac, H3K18ac and H4K8ac level**
669 To classify nuclei in the wing pouch according to cell cycle phase and to quantitatively correlate levels
670 of H3 and acetylation levels with each phase, a custom image analysis workflow was implemented in
671 ImageJ/Fiji. A single z-slice containing the highest number of pouch cells was selected from each
672 control disc. The image stack was split into individual channels (e.g., DAPI, GFP-E2f1$^{1-230}$, mRFP-NLS-
673 CycB$^{1-266}$, H3K27ac). To generate a nuclear mask, the DAPI, GFP, RFP, and other nuclear markers
674 were averaged sequentially using the Image Calculator. The resulting image was thresholded using the
675 Otsu method (upper limit set to 255) and converted into a binary mask defining nuclear pixels. A nuclear
676 pixel selection was generated from the binary image and added to the ROI Manager. The pouch region
677 was manually defined based on wing fold morphology. A binary “AND” operation was used to restrict
678 the nuclear pixel mask to the pouch, producing a final pouch-specific nuclear mask. This mask was
679 overlaid on the GFP, RFP, and other nuclear marker channels, and the X/Y coordinates of each ROI
680 were used to extract signal intensities for each nuclear pixel. Threshold values for GFP and RFP
681 determined based on average intensity of 5 nuclei in early S-phase. Each nuclear pixel was classified
682 into a cell cycle phase using these thresholds, following FUCCI-based criteria: G2 phase: GFP >
683 threshold, RFP > threshold; G1 phase: GFP > threshold, RFP ≤ threshold; Early/mid S phase: GFP ≤
684 threshold, RFP ≤ threshold; Late S phase: GFP ≤ threshold, RFP > threshold. For each nuclear pixel,
685 the intensity of the corresponding nuclear markers (e.g., H3, acetyl-lysine, H3K27ac) was recorded. To

686 account for inter-sample variability, intensity values within each cell cycle phase were normalized by
687 dividing them by the total nuclear marker signal summed across all phases (G1, early S, late S, and
688 G2) within the same disc. This normalization provided the relative contribution of each cell cycle phase
689 to the total signal, allowing for direct comparisons across samples.
690
691 **γH2Av intensity quantifications**
692 To create a nuclear mask, an xy- representation containing the maximum number of pouch nuclei was
693 generated using a sum projection of the DAPI channel. The background signal was reduced using the
694 "Subtract Background" function with a rolling ball radius of 100 pixels. Local contrast was enhanced
695 with the "Enhance Local Contrast (CLAHE)" function, using a block size of 127, 256 histogram bins,
696 and a maximum slope of 3. Automatic thresholding was performed using the "Moments" method with
697 the "dark" option selected, and the image was then converted into a binary mask. A nuclear ROI was
698 generated from this mask using the selection tool. The pouch region was manually selected based on
699 wing fold morphology. To isolate the nuclear pixels within the pouch, a binary "AND" operation was
700 used to combine nuclear mask and pouch selection. This final mask was used to measure γH2Av and
701 DAPI intensities for each disc. γH2Av intensities were normalized to the corresponding DAPI intensity.
702
703 **CUT&Tag Bioinformatic Analysis**
704 The CUT&Tag data processing was performed as described before with some modifications
705 (Atinbayeva et al., 2024, Ibarra-Morales et al., 2021, Cardamone et al., 2025). As our quantitative
706 CUT&Tag sequencing libraries contained DNA from *D. melanogaster* and spike-in of *lambda* phage
707 genome (Genbank: J02459.1), we mapped the raw paired-end reads to a constructed hybrid dm6 and
708 *Lambda* phage genome using *snakePipes-v3.0.0 DNA-mapping* (Bhardwaj et al., 2019) with updated
709 Bowtie2 mapping parameters, as well as adapter trimming and MAPQ ≥ 1 filtering (*DNAmapping --mapq*
710 *1 --trim --fastqc --properPairs --dedup --cutntag --DAG --alignerOpts='--local --very-sensitive-local --no-*
711 *discordant --no-mixed -I 10 -X 700'*). To assess reproducibility of both replicates, we utilised the
712 *multiBamSummary* and *plotCorrelation* from *deepTools-v.2.5.7* to compute the Spearman correlation
713 between the two replicates. Aligned replicates were merged before normalization to both H3 and spike-
714 in signals. The code used for the H3 and *Lambda* normalization analysis was based on work done by
715 Yinxiu Zhan (https://github.com/zhanyinx/atinbayeva_paper_2023) for (Atinbayeva et al., 2024).
716 CUT&Tag peaks were called using *snakePipes-v3.0.0 ChIPseq* with *MACS2-v 2.2.9.1* (*ChIPseq -d*
717 *Output_spikein hybrid.yaml H3_spikein_config.yaml --peakCaller MACS2 --cutntag --*
718 *peakCallerOptions "--broad --qvalue 0.5 -f BAMPE" --DAG*). Normalized bigWig and bam files were
719 generated with *deepTools-v3.5.6* and used to compute matrices of signal enrichment +/− 5kb around
720 transcription start sites (TSS) or peak centers of shared or unique peaks for *wt* and *Cdk1KD*. Coverage
721 heatmaps and profiles were created using *plotHeatmap* or *plotProfile* from *deepTools-v.2.5.7*.
722 For the quantification, the number of PE reads were counted in each shared or unique peak for *wt* and
723 *Cdk1KD* (*multiBamSummary BED-file --bamfiles <input files> --extendReads --outRawCounts <file>*)
724 as well as in 500 bp bins across the dm6 genome (*multiBamSummary bins --bamfiles <input files> --*
725 *binSize 500 --extendReads --outRawCounts <file>*). The *DESeq2-v1.38.3* analysis was performed

using the previously computed H3 and spike-in scaling factors from merged data for size factor. Bins and peaks with basemean (average read count across samples) of less than or equal to 25 read counts were discarded. The design matrix was setup to compare the samples by condition and correct for replicate effects (*design = ~replicate + condition*). Finally, we executed the *DESeq2* shrinkage of log2 fold changes (*type = 'normal'*).

CODE AND DATA AVAILABILITY

All data, workflows and FIJI based algorithms necessary to interpret the imaging data are included within the manuscript. Original imaging data and any additional information required to reanalyze the data reported in this paper will be shared by AKC upon request. The code used for the mapping, normalization, peak calling and signal quantification is available on Github: https://github.com/LaraH9/nogay_et_al_2025. The CUT&Tag sequencing data generated in this study is provided on NCBI SRA: https://www.ncbi.nlm.nih.gov/sra/PRJNA1300380.

AUTHOR CONTRIBUTIONS

Conceptualization LN, AKC; Data curation LN, LH, AKC; Formal analysis LN, LH, AKC; Funding acquisition AKC; Investigation LN, AVM; Methodology LN, AVM, FC, IG, AS, AF, LE, AKC; Project administration IG, AKC; Supervision NI, AKC; Validation LN, AVM, FC, IG; Visualization LN, LH, AKC; Writing – original draft LN, AKC; Writing – review & editing LN, AVM, AKC

ACKNOWLEDGEMENTS

We thank the staff of the Life Imaging Center (LIC) in the Hilde Mangold House (HMH) of the Albert-Ludwigs-University of Freiburg for help with their confocal microscopy resources, and the excellent support in image recording. We specifically thank the DFG for supporting our imaging work through project number 414136422. We thank the Bioinformatics and Sequencing facilities at the MPI-IE for supporting this work. We thank Galina Erikson for supporting our bioinformatic analysis. We thank Laura Bauttita, Melissa Harrison, Iswar Hariharan, Dirk Bohmann and Jürg Müller for sharing reagents and the Bloomington *Drosophila* Stock Center (BDSC), the Vienna *Drosophila* Stock Collection (VDRC), the University of Zurich ORFeome Project (FlyORF) and the Developmental Studies Hybridoma Bank (DSHB) for providing fly stocks and antibodies. We thank the IMPRS-EBM and SGBM graduate schools for supporting our doctoral researchers.

FUNDING

Funding for this work was provided by the Deutsche Forschungsgemeinschaft (DFG, German Research Foundation) under Germany´s Excellence Strategy (CIBSS – EXC-2189), the DFG Heisenberg Program to AKC (668189), as well as DFG grants to AKC (667603) and the Boehringer Ingelheim

Foundation (BIF Plus3 & Rise Up) to AKC. The funders had no role in study design, data collection and analysis, decision to publish, or preparation of the manuscript.

DECLARATION OF INTEREST

The authors declare no competing interests.

773 **REFERENCES**

774

775 AAGAARD, L., LAIBLE, G., SELENKO, P., SCHMID, M., DORN, R., SCHOTTA, G., KUHFITTIG, S., WOLF, A.,
776 LEBERSORGER, A., SINGH, P. B., REUTER, G. & JENUWEIN, T. 1999. Functional mammalian
777 homologues of the Drosophila PEV-modifier Su(var)3-9 encode centromere-associated proteins which
778 complex with the heterochromatin component M31. *EMBO J,* 18**,** 1923-38.

779 AGGARWAL, B. D. & CALVI, B. R. 2004. Chromatin regulates origin activity in Drosophila follicle cells. *Nature,*
780 430**,** 372-6.

781 AIT-SI-ALI, S., RAMIREZ, S., BARRE, F. X., DKHISSI, F., MAGNAGHI-JAULIN, L., GIRAULT, J. A., ROBIN, P.,
782 KNIBIEHLER, M., PRITCHARD, L. L., DUCOMMUN, B., TROUCHE, D. & HAREL-BELLAN, A. 1998.
783 Histone acetyltransferase activity of CBP is controlled by cycle-dependent kinases and oncoprotein E1A.
784 *Nature,* 396**,** 184-6.

785 ALABERT, C., BARTH, T. K., REVERON-GOMEZ, N., SIDOLI, S., SCHMIDT, A., JENSEN, O. N., IMHOF, A. &
786 GROTH, A. 2015. Two distinct modes for propagation of histone PTMs across the cell cycle. *Genes Dev,*
787 29**,** 585-90.

788 ALABERT, C. & GROTH, A. 2012. Chromatin replication and epigenome maintenance. *Nat Rev Mol Cell Biol,* 13**,**
789 153-67.

790 ANNUNZIATO, A. T. 2015. The Fork in the Road: Histone Partitioning During DNA Replication. *Genes (Basel),* 6**,**
791 353-71.

792 ANNUNZIATO, A. T. & HANSEN, J. C. 2000. Role of histone acetylation in the assembly and modulation of
793 chromatin structures. *Gene Expr,* 9**,** 37-61.

794 ANNUNZIATO, A. T. & SEALE, R. L. 1983. Histone deacetylation is required for the maturation of newly replicated
795 chromatin. *J Biol Chem,* 258**,** 12675-84.

796 ATINBAYEVA, N., VALENT, I., ZENK, F., LOESER, E., RAUER, M., HERUR, S., QUARATO, P., PYROWOLAKIS,
797 G., GOMEZ-AULI, A., MITTLER, G., CECERE, G., ERHARDT, S., TIANA, G., ZHAN, Y. & IOVINO, N.
798 2024. Inheritance of H3K9 methylation regulates genome architecture in Drosophila early embryos. *EMBO*
799 *J,* 43**,** 2685-2714.

800 BARRETO-GALVEZ, A., NILJIKAR, M., GAGLIARDI, J., ZHANG, R., KUMAR, V., JURUWALA, A., PRADEEP, A.,
801 SHAIKH, A., TIWARI, P., SHARMA, K., GERHARDT, J., CAO, J., KATAOKA, K., DURBIN, A., QI, J., YE,
802 B. H. & MADIREDDY, A. 2023. Acetyl transferase EP300 deficiency leads to chronic replication stress
803 mediated by defective fork protection at stalled replication forks. *bioRxiv*.

804 BENSON, L. J., GU, Y., YAKOVLEVA, T., TONG, K., BARROWS, C., STRACK, C. L., COOK, R. G., MIZZEN, C.
805 A. & ANNUNZIATO, A. T. 2006. Modifications of H3 and H4 during chromatin replication, nucleosome
806 assembly, and histone exchange. *J Biol Chem,* 281**,** 9287-96.

807 BEUCHLE, D., STRUHL, G. & MULLER, J. 2001. Polycomb group proteins and heritable silencing of Drosophila
808 Hox genes. *Development,* 128**,** 993-1004.

809 BHARDWAJ, V., HEYNE, S., SIKORA, K., RABBANI, L., RAUER, M., KILPERT, F., RICHTER, A. S., RYAN, D. P.
810 & MANKE, T. 2019. snakePipes: facilitating flexible, scalable and integrative epigenomic analysis.
811 *Bioinformatics,* 35**,** 4757-4759.

812 BHATNAGAR, A., KARNAY, A. M. & ELEFANT, F. 2023. Drosophila Epigenetics. *Handbook of Epigenetics.*

813 BLACKLEDGE, N. P. & KLOSE, R. J. 2021. The molecular principles of gene regulation by Polycomb repressive
814 complexes. *Nat Rev Mol Cell Biol,* 22**,** 815-833.

815 BOIJA, A., MAHAT, D. B., ZARE, A., HOLMQVIST, P. H., PHILIP, P., MEYERS, D. J., COLE, P. A., LIS, J. T.,
816 STENBERG, P. & MANNERVIK, M. 2017. CBP Regulates Recruitment and Release of Promoter-
817 Proximal RNA Polymerase II. *Mol Cell,* 68**,** 491-503 e5.

818 BROOKES, E. & SHI, Y. 2014. Diverse epigenetic mechanisms of human disease. *Annu Rev Genet,* 48**,** 237-68.

819 BUENROSTRO, J. D., WU, B., LITZENBURGER, U. M., RUFF, D., GONZALES, M. L., SNYDER, M. P., CHANG,
820 H. Y. & GREENLEAF, W. J. 2015. Single-cell chromatin accessibility reveals principles of regulatory
821 variation. *Nature,* 523**,** 486-90.

822 BUTTITTA, L. A. & EDGAR, B. A. 2007. Mechanisms controlling cell cycle exit upon terminal differentiation. *Curr*
823 *Opin Cell Biol,* 19**,** 697-704.

824 BUTTITTA, L. A., KATZAROFF, A. J., PEREZ, C. L., DE LA CRUZ, A. & EDGAR, B. A. 2007. A double-assurance
825 mechanism controls cell cycle exit upon terminal differentiation in Drosophila. *Dev Cell,* 12**,** 631-43.

826 CAO, R., WANG, L., WANG, H., XIA, L., ERDJUMENT-BROMAGE, H., TEMPST, P., JONES, R. S. & ZHANG, Y.
827 2002. Role of histone H3 lysine 27 methylation in Polycomb-group silencing. *Science,* 298**,** 1039-43.

828 CARDAMONE, F., PIVA, A., LOSER, E., EICHENBERGER, B., ROMERO-MULERO, M. C., ZENK, F., SHIELDS,
829 E. J., CABEZAS-WALLSCHEID, N., BONASIO, R., TIANA, G., ZHAN, Y. & IOVINO, N. 2025. Chromatin
830 landscape at cis-regulatory elements orchestrates cell fate decisions in early embryogenesis. *Nat*
831 *Commun,* 16**,** 3007.

832 CAVALLI, G. & HEARD, E. 2019. Advances in epigenetics link genetics to the environment and disease. *Nature,*
833 571**,** 489-499.

834 CAZZALINI, O., SOMMATIS, S., TILLHON, M., DUTTO, I., BACHI, A., RAPP, A., NARDO, T., SCOVASSI, A. I.,
835 NECCHI, D., CARDOSO, M. C., STIVALA, L. A. & PROSPERI, E. 2014. CBP and p300 acetylate PCNA
836 to link its degradation with nucleotide excision repair synthesis. *Nucleic Acids Res,* 42**,** 8433-48.

837 CHEN, Y. C., KOUTELOU, E. & DENT, S. Y. R. 2022. Now open: Evolving insights to the roles of lysine acetylation
838 in chromatin organization and function. *Mol Cell,* 82**,** 716-727.

839 CIABRELLI, F., RABBANI, L., CARDAMONE, F., ZENK, F., LOSER, E., SCHACHTLE, M. A., MAZINA, M.,
840 LOUBIERE, V. & IOVINO, N. 2023. CBP and Gcn5 drive zygotic genome activation independently of their
841 catalytic activity. *Sci Adv,* 9**,** eadf2687.

842 CLASSEN, A. K., BUNKER, B. D., HARVEY, K. F., VACCARI, T. & BILDER, D. 2009. A tumor suppressor activity
843 of Drosophila Polycomb genes mediated by JAK-STAT signaling. *Nat Genet,* 41**,** 1150-5.

844 COSOLO, A., JAISWAL, J., CSORDAS, G., GRASS, I., UHLIROVA, M. & CLASSEN, A. K. 2019. JNK-dependent
845 cell cycle stalling in G2 promotes survival and senescence-like phenotypes in tissue stress. *Elife,* 8.

846 CRUCIANELLI, C., JAISWAL, J., VIJAYAKUMAR MAYA, A., NOGAY, L., COSOLO, A., GRASS, I. & CLASSEN,
847 A. K. 2022. Distinct signaling signatures drive compensatory proliferation via S-phase acceleration. *PLoS*
848 *Genet,* 18**,** e1010516.

849 DE MORREE, A. & RANDO, T. A. 2023. Regulation of adult stem cell quiescence and its functions in the
850 maintenance of tissue integrity. *Nat Rev Mol Cell Biol,* 24**,** 334-354.

851 DUTTO, I., SCALERA, C. & PROSPERI, E. 2018. CREBBP and p300 lysine acetyl transferases in the DNA
852 damage response. *Cell Mol Life Sci,* 75**,** 1325-1338.

853 EATON, M. L., PRINZ, J. A., MACALPINE, H. K., TRETYAKOV, G., KHARCHENKO, P. V. & MACALPINE, D. M.
854 2011. Chromatin signatures of the Drosophila replication program. *Genome Res,* 21**,** 164-74.

855 EBERT, A., SCHOTTA, G., LEIN, S., KUBICEK, S., KRAUSS, V., JENUWEIN, T. & REUTER, G. 2004. Su(var)
856 genes regulate the balance between euchromatin and heterochromatin in Drosophila. *Genes Dev,* 18**,**
857 2973-83.

858 ESCOBAR, T. M., LOYOLA, A. & REINBERG, D. 2021. Parental nucleosome segregation and the inheritance of
859 cellular identity. *Nat Rev Genet,* 22**,** 379-392.

860 ESCOBAR, T. M., OKSUZ, O., SALDANA-MEYER, R., DESCOSTES, N., BONASIO, R. & REINBERG, D. 2019.
861 Active and Repressed Chromatin Domains Exhibit Distinct Nucleosome Segregation during DNA
862 Replication. *Cell,* 179**,** 953-963 e11.

863 FALBO, K. B. & SHEN, X. 2009. Histone modifications during DNA replication. *Mol Cells,* 28**,** 149-54.

864 FEINBERG, A. P., KOLDOBSKIY, M. A. & GONDOR, A. 2016. Epigenetic modulators, modifiers and mediators in
865 cancer aetiology and progression. *Nat Rev Genet,* 17**,** 284-99.

866 FLOC'HLAY, S., BALAJI, R., STANKOVIC, D., CHRISTIAENS, V. M., BRAVO GONZALEZ-BLAS, C., DE
867 WINTER, S., HULSELMANS, G. J., DE WAEGENEER, M., QUAN, X., KOLDERE, D., ATKINS, M.,
868 HALDER, G., UHLIROVA, M., CLASSEN, A. K. & AERTS, S. 2023. Shared enhancer gene regulatory
869 networks between wound and oncogenic programs. *Elife,* 12.

870 FLURY, V. & GROTH, A. 2024. Safeguarding the epigenome through the cell cycle: a multitasking game. *Curr*
871 *Opin Genet Dev,* 85**,** 102161.

872 HERNANDEZ-SEGURA, A., NEHME, J. & DEMARIA, M. 2018. Hallmarks of Cellular Senescence. *Trends Cell*
873 *Biol,* 28**,** 436-453.

874 HOLMQVIST, P. H. & MANNERVIK, M. 2013. Genomic occupancy of the transcriptional co-activators p300 and
875 CBP. *Transcription,* 4**,** 18-23.

876 HUA, B. L. & ORR-WEAVER, T. L. 2017. DNA Replication Control During Drosophila Development: Insights into
877 the Onset of S Phase, Replication Initiation, and Fork Progression. *Genetics,* 207**,** 29-47.

878 HUANG, W., HICKSON, L. J., EIRIN, A., KIRKLAND, J. L. & LERMAN, L. O. 2022. Cellular senescence: the good,
879 the bad and the unknown. *Nat Rev Nephrol,* 18**,** 611-627.

880 IBARRA-MORALES, D., RAUER, M., QUARATO, P., RABBANI, L., ZENK, F., SCHULTE-SASSE, M.,
881 CARDAMONE, F., GOMEZ-AULI, A., CECERE, G. & IOVINO, N. 2021. Histone variant H2A.Z regulates
882 zygotic genome activation. *Nat Commun,* 12**,** 7002.

883 ITO, T. & IGAKI, T. 2021. Yorkie drives Ras-induced tumor progression by microRNA-mediated inhibition of cellular
884 senescence. *Sci Signal,* 14.

885 JACKSON, V., SHIRES, A., TANPHAICHITR, N. & CHALKLEY, R. 1976. Modifications to histones immediately
886 after synthesis. *J Mol Biol,* 104**,** 471-83.

887 JAISWAL, J., EGERT, J., ENGESSER, R., PEYROTON, A. A., NOGAY, L., WEICHSELBERGER, V.,
888 CRUCIANELLI, C., GRASS, I., KREUTZ, C., TIMMER, J. & CLASSEN, A. K. 2023. Mutual repression

889 between JNK/AP-1 and JAK/STAT stratifies senescent and proliferative cell behaviors during tissue
890 regeneration. *PLoS Biol,* 21**,** e3001665.

891 JOHNSTON, L. A. & EDGAR, B. A. 1998. Wingless and Notch regulate cell-cycle arrest in the developing
892 Drosophila wing. *Nature,* 394**,** 82-4.

893 KHAN, C., MULIYIL, S., AYYUB, C. & RAO, B. J. 2017. The initiator caspase Dronc plays a non-apoptotic role in
894 promoting DNA damage signalling in D. melanogaster. *J Cell Sci,* 130**,** 2984-2995.

895 LANDE-DINER, L., ZHANG, J. & CEDAR, H. 2009. Shifts in replication timing actively affect histone acetylation
896 during nucleosome reassembly. *Mol Cell,* 34**,** 767-74.

897 LEE, L. A. & ORR-WEAVER, T. L. 2003. Regulation of cell cycles in Drosophila development: intrinsic and extrinsic
898 cues. *Annu Rev Genet,* 37**,** 545-78.

899 LI, Q., ZHOU, H., WURTELE, H., DAVIES, B., HORAZDOVSKY, B., VERREAULT, A. & ZHANG, Z. 2008.
900 Acetylation of histone H3 lysine 56 regulates replication-coupled nucleosome assembly. *Cell,* 134**,** 244-
901 55.

902 LIU, W., TANASA, B., TYURINA, O. V., ZHOU, T. Y., GASSMANN, R., LIU, W. T., OHGI, K. A., BENNER, C.,
903 GARCIA-BASSETS, I., AGGARWAL, A. K., DESAI, A., DORRESTEIN, P. C., GLASS, C. K. &
904 ROSENFELD, M. G. 2010. PHF8 mediates histone H4 lysine 20 demethylation events involved in cell
905 cycle progression. *Nature,* 466**,** 508-12.

906 LOPEZ-HERNANDEZ, L., TOOLAN-KERR, P., BANNISTER, A. J. & MILLAN-ZAMBRANO, G. 2025. Dynamic
907 histone modification patterns coordinating DNA processes. *Mol Cell,* 85**,** 225-237.

908 MA, Y., KANAKOUSAKI, K. & BUTTITTA, L. 2015. How the cell cycle impacts chromatin architecture and
909 influences cell fate. *Front Genet,* 6**,** 19.

910 MADIGAN, J. P., CHOTKOWSKI, H. L. & GLASER, R. L. 2002. DNA double-strand break-induced phosphorylation
911 of Drosophila histone variant H2Av helps prevent radiation-induced apoptosis. *Nucleic Acids Res,* 30**,**
912 3698-705.

913 MARSH, A. J., PIROGOV, S., KAUR, Y., RUFFRIDGE, A. J., SAJWAN, S., GIBSON, T. J., HUNT, G., HARRISON,
914 M. M. & MANNERVIK, M. 2025. Catalytic-dependent and independent functions of the histone
915 acetyltransferase CBP promote pioneer-factor-mediated zygotic genome activation. *Mol Cell*.

916 MASUMOTO, H., HAWKE, D., KOBAYASHI, R. & VERREAULT, A. 2005. A role for cell-cycle-regulated histone
917 H3 lysine 56 acetylation in the DNA damage response. *Nature,* 436**,** 294-8.

918 MATTHEWS, H. K., BERTOLI, C. & DE BRUIN, R. A. M. 2022. Cell cycle control in cancer. *Nat Rev Mol Cell Biol,*
919 23**,** 74-88.

920 MAYA, A. V., NOGAY, L., HECKMANN, L., GRASS, I., KIERDORF, K., BüSCHER, J. & CLASSEN, A.-K. 2024.
921 PDK-1/S6K and mTORC1 bypass systemic growth restrictions to promote regeneration. *bioRxiv***,**
922 2024.08.05.606658.

923 MCCONNELL, K. H., DIXON, M. & CALVI, B. R. 2012. The histone acetyltransferases CBP and Chameau integrate
924 developmental and DNA replication programs in Drosophila ovarian follicle cells. *Development,* 139**,** 3880-
925 90.

926 MENDIRATTA, S., GATTO, A. & ALMOUZNI, G. 2019. Histone supply: Multitiered regulation ensures chromatin
927 dynamics throughout the cell cycle. *J Cell Biol,* 218**,** 39-54.

928 MILAN, M., CAMPUZANO, S. & GARCIA-BELLIDO, A. 1996. Cell cycling and patterned cell proliferation in the
929 wing primordium of Drosophila. *Proc Natl Acad Sci U S A,* 93**,** 640-5.

930 MILLAN-ZAMBRANO, G., BURTON, A., BANNISTER, A. J. & SCHNEIDER, R. 2022. Histone post-translational
931 modifications - cause and consequence of genome function. *Nat Rev Genet,* 23**,** 563-580.

932 MULLER, J., GAUNT, S. & LAWRENCE, P. A. 1995. Function of the Polycomb protein is conserved in mice and
933 flies. *Development,* 121**,** 2847-52.

934 NARITA, M., NUNEZ, S., HEARD, E., NARITA, M., LIN, A. W., HEARN, S. A., SPECTOR, D. L., HANNON, G. J.
935 & LOWE, S. W. 2003. Rb-mediated heterochromatin formation and silencing of E2F target genes during
936 cellular senescence. *Cell,* 113**,** 703-16.

937 NEUFELD, T. P., DE LA CRUZ, A. F., JOHNSTON, L. A. & EDGAR, B. A. 1998. Coordination of growth and cell
938 division in the Drosophila wing. *Cell,* 93**,** 1183-93.

939 ODA, H., HUBNER, M. R., BECK, D. B., VERMEULEN, M., HURWITZ, J., SPECTOR, D. L. & REINBERG, D.
940 2010. Regulation of the histone H4 monomethylase PR-Set7 by CRL4(Cdt2)-mediated PCNA-dependent
941 degradation during DNA damage. *Mol Cell,* 40**,** 364-76.

942 OGIWARA, H., UI, A., OTSUKA, A., SATOH, H., YOKOMI, I., NAKAJIMA, S., YASUI, A., YOKOTA, J. & KOHNO,
943 T. 2011. Histone acetylation by CBP and p300 at double-strand break sites facilitates SWI/SNF chromatin
944 remodeling and the recruitment of non-homologous end joining factors. *Oncogene,* 30**,** 2135-46.

945 PADEKEN, J., METHOT, S. P. & GASSER, S. M. 2022. Establishment of H3K9-methylated heterochromatin and
946 its functions in tissue differentiation and maintenance. *Nat Rev Mol Cell Biol,* 23**,** 623-640.

947 PENGELLY, A. R., COPUR, O., JACKLE, H., HERZIG, A. & MULLER, J. 2013. A histone mutant reproduces the
948 phenotype caused by loss of histone-modifying factor Polycomb. *Science,* 339**,** 698-9.

949 PETERMANN, E., ORTA, M. L., ISSAEVA, N., SCHULTZ, N. & HELLEDAY, T. 2010. Hydroxyurea-stalled
950 replication forks become progressively inactivated and require two different RAD51-mediated pathways
951 for restart and repair. *Mol Cell,* 37**,** 492-502.

952 PETERSON, C. L. & LANIEL, M. A. 2004. Histones and histone modifications. *Curr Biol,* 14**,** R546-51.

953 PETRUK, S., BLACK, K. L., KOVERMANN, S. K., BROCK, H. W. & MAZO, A. 2013. Stepwise histone modifications
954 are mediated by multiple enzymes that rapidly associate with nascent DNA during replication. *Nat*
955 *Commun,* 4**,** 2841.

956 PETRUK, S., SEDKOV, Y., SMITH, S., TILLIB, S., KRAEVSKI, V., NAKAMURA, T., CANAANI, E., CROCE, C. M.
957 & MAZO, A. 2001. Trithorax and dCBP acting in a complex to maintain expression of a homeotic gene.
958 *Science,* 294**,** 1331-4.

959 PHILIP, P., BOIJA, A., VAID, R., CHURCHER, A. M., MEYERS, D. J., COLE, P. A., MANNERVIK, M. &
960 STENBERG, P. 2015. CBP binding outside of promoters and enhancers in Drosophila melanogaster.
961 *Epigenetics Chromatin,* 8**,** 48.

962 PROBER, D. A. & EDGAR, B. A. 2000. Ras1 promotes cellular growth in the Drosophila wing. *Cell,* 100**,** 435-46.

963 RAMADAN, W. S., AHMED, S. B. M., TALAAT, I. M., LOZON, L., MOUFFAK, S., GEMOLL, T., MANSOUR, W. Y.
964 & EL-AWADY, R. 2025. The histone acetyltransferase CBP participates in regulating the DNA damage
965 response through ATM after double-strand breaks. *Genome Biol,* 26**,** 89.

966 RAMOS-ALONSO, L. & CHYMKOWITCH, P. 2024. Maintaining transcriptional homeostasis during cell cycle.
967 *Transcription,* 15**,** 1-21.

968 REVERON-GOMEZ, N., GONZALEZ-AGUILERA, C., STEWART-MORGAN, K. R., PETRYK, N., FLURY, V.,
969 GRAZIANO, S., JOHANSEN, J. V., JAKOBSEN, J. S., ALABERT, C. & GROTH, A. 2018. Accurate
970 Recycling of Parental Histones Reproduces the Histone Modification Landscape during DNA Replication.
971 *Mol Cell,* 72**,** 239-249 e5.

972 RUIZ-CARRILLO, A., WANGH, L. J. & ALLFREY, V. G. 1975. Processing of newly synthesized histone molecules.
973 *Science,* 190**,** 117-28.

974 SCHINDELIN, J., ARGANDA-CARRERAS, I., FRISE, E., KAYNIG, V., LONGAIR, M., PIETZSCH, T., PREIBISCH,
975 S., RUEDEN, C., SAALFELD, S., SCHMID, B., TINEVEZ, J. Y., WHITE, D. J., HARTENSTEIN, V.,
976 ELICEIRI, K., TOMANCAK, P. & CARDONA, A. 2012. Fiji: an open-source platform for biological-image
977 analysis. *Nat Methods,* 9**,** 676-82.

978 SMITH-BOLTON, R. K., WORLEY, M. I., KANDA, H. & HARIHARAN, I. K. 2009. Regenerative growth in Drosophila
979 imaginal discs is regulated by Wingless and Myc. *Dev Cell,* 16**,** 797-809.

980 SMOLIK, S. & JONES, K. 2007. Drosophila dCBP is involved in establishing the DNA replication checkpoint. *Mol*
981 *Cell Biol,* 27**,** 135-46.

982 SOBEL, R. E., COOK, R. G., PERRY, C. A., ANNUNZIATO, A. T. & ALLIS, C. D. 1995. Conservation of deposition-
983 related acetylation sites in newly synthesized histones H3 and H4. *Proc Natl Acad Sci U S A,* 92**,** 1237-
984 41.

985 SPARMANN, A. & VAN LOHUIZEN, M. 2006. Polycomb silencers control cell fate, development and cancer. *Nat*
986 *Rev Cancer,* 6**,** 846-56.

987 STAUFFER, D., CHANG, B., HUANG, J., DUNN, A. & THAYER, M. 2007. p300/CREB-binding protein interacts
988 with ATR and is required for the DNA replication checkpoint. *J Biol Chem,* 282**,** 9678-9687.

989 STEIN, G., PARK, W., THRALL, C., MANS, R. & STEIN, J. 1975. Regulation of cell cycle stage-specific
990 transcription of histone genes from chromatin by non-histone chromosomal proteins. *Nature,* 257**,** 764-7.

991 STEWART-MORGAN, K. R., PETRYK, N. & GROTH, A. 2020. Chromatin replication and epigenetic cell memory.
992 *Nat Cell Biol,* 22**,** 361-371.

993 TAPON, N., MOBERG, K. H. & HARIHARAN, I. K. 2001. The coupling of cell growth to the cell cycle. *Curr Opin*
994 *Cell Biol,* 13**,** 731-7.

995 TESSARZ, P. & KOUZARIDES, T. 2014. Histone core modifications regulating nucleosome structure and
996 dynamics. *Nat Rev Mol Cell Biol,* 15**,** 703-8.

997 TIE, F., BANERJEE, R., FU, C., STRATTON, C. A., FANG, M. & HARTE, P. J. 2016. Polycomb inhibits histone
998 acetylation by CBP by binding directly to its catalytic domain. *Proc Natl Acad Sci U S A,* 113**,** E744-53.

999 TIE, F., BANERJEE, R., STRATTON, C. A., PRASAD-SINHA, J., STEPANIK, V., ZLOBIN, A., DIAZ, M. O.,
1000 SCACHERI, P. C. & HARTE, P. J. 2009. CBP-mediated acetylation of histone H3 lysine 27 antagonizes
1001 Drosophila Polycomb silencing. *Development,* 136**,** 3131-41.

1002 TILLHON, M., CAZZALINI, O., NARDO, T., NECCHI, D., SOMMATIS, S., STIVALA, L. A., SCOVASSI, A. I. &
1003 PROSPERI, E. 2012. p300/CBP acetyl transferases interact with and acetylate the nucleotide excision
1004 repair factor XPG. *DNA Repair (Amst),* 11**,** 844-52.

1005 TROUTH, A., RAVICHANDRAN, K., GAFKEN, P. R., MARTIRE, S., BOYLE, G. E., VERONEZI, G. M. B., LA, V.,
1006 NAMCIU, S. J., BANASZYNSKI, L. A., SARTHY, J. F. & RAMACHANDRAN, S. 2025. The length of the
1007 G1 phase is an essential determinant of H3K27me3 landscapes across diverse cell types. *PLoS Biol,* 23**,**
1008 e3003119.

1009 TROVATO, M., PATIL, V., GEHRE, M. & NOH, K. M. 2020. Histone Variant H3.3 Mutations in Defining the
1010 Chromatin Function in Mammals. *Cells,* 9.

1011 VERREAULT, A., KAUFMAN, P. D., KOBAYASHI, R. & STILLMAN, B. 1998. Nucleosomal DNA regulates the
1012 core-histone-binding subunit of the human Hat1 acetyltransferase. *Curr Biol,* 8**,** 96-108.

1013 WENGER, A., BIRAN, A., ALCARAZ, N., REDO-RIVEIRO, A., SELL, A. C., KRAUTZ, R., FLURY, V., REVERON-
1014 GOMEZ, N., SOLIS-MEZARINO, V., VOLKER-ALBERT, M., IMHOF, A., ANDERSSON, R., BRICKMAN,
1015 J. M. & GROTH, A. 2023. Symmetric inheritance of parental histones governs epigenome maintenance
1016 and embryonic stem cell identity. *Nat Genet,* 55**,** 1567-1578.

1017 WILLNOW, P. & TELEMAN, A. A. 2024. Nuclear position and local acetyl-CoA production regulate chromatin state.
1018 *Nature,* 630**,** 466-474.

1019 YAO, T. P., OH, S. P., FUCHS, M., ZHOU, N. D., CH'NG, L. E., NEWSOME, D., BRONSON, R. T., LI, E.,
1020 LIVINGSTON, D. M. & ECKNER, R. 1998. Gene dosage-dependent embryonic development and
1021 proliferation defects in mice lacking the transcriptional integrator p300. *Cell,* 93**,** 361-72.

1022 ZANG, Y., YOSHIMOTO, M. & IGAKI, T. 2025. Programmed cell senescence is required for sensory organ
1023 development in Drosophila. *iScience,* 28**,** 112048.

1024 ZEE, B. M., BRITTON, L. M., WOLLE, D., HABERMAN, D. M. & GARCIA, B. A. 2012. Origins and formation of
1025 histone methylation across the human cell cycle. *Mol Cell Biol,* 32**,** 2503-14.

1026 ZENK, F., CARDAMONE, F., IBARRA MORALES, D. A., ATINBAYEVA, N., ZHAN, Y. & IOVINO, N. 2023.
1027 Analyzing the Genome-Wide Distribution of Histone Marks by CUT&Tag in Drosophila Embryos. *Methods*
1028 *Mol Biol,* 2655**,** 1-17.

1029 ZHOU, C. Y. & HEALD, R. 2020. Emergent properties of mitotic chromosomes. *Curr Opin Cell Biol,* 64**,** 43-49.

1030 ZIELKE, N., KORZELIUS, J., VAN STRAATEN, M., BENDER, K., SCHUHKNECHT, G. F. P., DUTTA, D., XIANG,
1031 J. & EDGAR, B. A. 2014. Fly-FUCCI: A versatile tool for studying cell proliferation in complex tissues. *Cell*
1032 *Rep,* 7**,** 588-598.
1033

1034

1035 **Table S1 Experimental strains, reagents and software**

1036

Tool	Source	ID
w^{118}	David Bilder, University of California, Berkeley	FBal0018157
UAS-GFP^{S56T}	Bloomington *Drosophila* Stock Center	BDSC: 1521
$rn^{GAL4\text{-}DeltaS}$, tubGAL80^{ts}	Bloomington *Drosophila* Stock Center	BDSC: 8142; 7018 recombinant
$rn^{GAL4\text{-}5}$, UAS-egr, tubP-GAL80^{ts}	Iswar Hariharan, University of California, Berkeley	BDSC: 8142; 7018 recombinant
'E2F1-FUCCI, CycB-FUCCI'; Ubi-GFP.E2f1$^{1\text{-}230}$, Ubi-mRFP1.NLS.CycB$^{1\text{-}266}$	Bloomington *Drosophila* Stock Center	BDSC: 55123
UAS-Cdk1 RNAi [TRiP.HMS01531]	Bloomington *Drosophila* Stock Center	BDSC: 36117
lf/CyO-GFP; UAS-E2F, UAS-DP/TM6b	Laura Buttitta, University of Michigan	PMID: 9657151
UAS-pnt.P1	Bloomington *Drosophila* Stock Center	BDSC: 869
UAS-E(z)-RNAi (TRiP.HMS00066)	Bloomington *Drosophila* Stock Center	BDSC: 33659
UAS-nejire-RNAi(TRiP.HMS01507)	Bloomington *Drosophila* Stock Center	BDSC: 37489
UAS-InR-DA (UAS-InR.A1325D)	Bloomington *Drosophila* Stock Center	BDSC: 8263
'TRE-RFP': TRE-DsRed.T4	Dirk Bohmann, University of Rochester Medical Center	PMID: 22509270
UAS-nejire	Bloomington *Drosophila* Stock Center	BDSC: 32573
UAS-HDAC1-RNAi (TRiP.HMS00607)	Bloomington *Drosophila* Stock Center	BDSC: 33725
CBP-GFP	Melissa Harrison, University of Wisconsin School of Medicine and Public Health	PMID: 40441155
w; Df(2L)HisC FRT40A/CyO, twi-GAL4, UAS-GFP; 6xHisGU^{H3K27R}/6xHisGU^{H3K27R}	Jürg Müller, Max Planck Institute of Biochemistry	PMID: 23393264

yw hs-flp122; hs-nGFP FRT40A; 6xHisGU$^{H3\text{-}K27R}$/SM5^TM6B	Jürg Müller, Max Planck Institute of Biochemistry	PMID: 23393264
hs-flp122; FRT40A ubi-GFP/CyO (GFP); Dr/TM6c		
UAS-bsk[DN]	Bloomington *Drosophila* Stock Center	BDSC: 6409
Chicken anti-GFP	Abcam	Cat. #: ab13970
Rabbit monoclonal anti-GFP	Invitrogen	Cat. #: G10362
Rat monoclonal anti-RFP	ChromoTek	Cat. #: 5F8 RRID: AB_2336064
Rabbit polyclonal anti-H3K9ac	Active motif	Cat. #: 39017 RRID: AB_2616593
Rabbit polyclonal anti-H4K8ac	Active motif	Cat. #: 61104 RRID: AB_2793506
Rabbit polyclonal anti-acetyl Lysine	Abcam	Cat. #: ab80178
Rabbit monoclonal anti-crotonyl Histone H3	PTMab	Cat. #: PTM-517RM
Rabbit polyclonal anti-H3K9me1me2me3	Active motif	Cat. #: 39242 RRID: AB_2793200
Rabbit polyclonal anti-H3K18ac	Active motif	Cat. #: 39756 RRID: AB_2714186
Mouse monoclonal anti-H3K27ac	Active motif	Cat. #: 39085 RRID: AB_2793305
Rabbit polyclonal anti-H3K4me3	Abcam	Cat. #: ab8580
Mouse monoclonal anti-H3K27me3	Abcam	Cat. #: ab6002
Rabbit polyclonal anti-H3K9me3	Abcam	Cat. #: ab8898
Rabbit polyclonal anti-H3	Abcam	Cat. #: ab1791
Rabbit polyclonal anti-Histone H2AvD phosphoS137	Rockland	Cat. #: 600-401-914
Mouse monoclonal anti-Cut	DSHB	Cat. #: 2B10 RRID: AB_528186
Mouse monoclonal anti-Engrailed/Invected	DSHB	Cat. #: 4D9 RRID: AB_528224
Mouse monoclonal anti-Nubbin	DSHB	Cat. #: 2D4 RRID: AB_2722119
Mouse monoclonal anti-Antp	DSHB	Cat. #: 8C11 RRID: AB_528083
Mouse monoclonal anti-Ptc	DSHB	Cat. #: Apa1

		RRID: AB_528441
Mouse monoclonal anti Abd-B	DSHB	Cat. #: 1A2E9 RRID: AB_528061
Mouse monoclonal anti-Wg	DSHB	Cat. #: 4D4 RRID: AB_528512
Mouse monoclonal anti-Histone H3 (for CUT&Tag)	Active motif	Cat. #: 39763 RRID: AB_2650522
Rabbit polyclonal anti-H3K27ac (for CUT&Tag)	Diagenode	Cat. #: C15410196
Rabbit polyclonal anti-H3K27me3 (for CUT&Tag)	Diagendoe	Cat. #: C15410195
Rabbit monoclonal anti-H3K9me3 (for CUT&Tag)	Abcam	Cat. #: ab176916
DAPI	Sigma Aldrich	Cat #: D9564
Goat anti-mouse IgG Alexa Flour 488	Invitrogen	Cat. #: A-11001
Goat anti-chicken IgY Alexa Flour 488	Invitrogen	Cat. #: A-11039
Goat anti-rabbit IgG Alexa Flour 488	Invitrogen	Cat. #: A-11008
Goat anti-mouse IgG Alexa Flour 555	Invitrogen	Cat. #: A-21422
Goat anti-rat IgG Alexa Flour 555	Invitrogen	Cat. #: A-21434
Goat anti-mouse Alexa Flour 647	Invitrogen	Cat. #: A-21235
Donkey anti-mouse Alexa Flour 647 preabsorbed	Abcam	Cat. #: ab150111
Goat anti-rat Alexa Flour 647	Invitrogen	Cat. #: A-21247
Goat anti-rabbit Alexa Flour 647	Invitrogen	Cat. #: A-21244
Click-iT Plus EdU Alexa Fluor 647 Imaging Kit	Invitrogen	Cat. #: C10640
Click-iT Plus OPP Alexa Fluor 647 Imaging Kit	Invitrogen	Cat. #: C10458
CellEvent Senescence Green Detection Kit	Invitrogen	Cat. #: C10850
FIJI (ImageJ 1.54f)	(Schindelin et al., 2012)	https://fiji.sc/
GraphPad Prism	Graph Pad	version 9.5.0
Affinity Designer	Affinity	Up to version 2.6.3
Biorender	Science Suite Inc. DBA BioRender	Biorender

1041 **MAIN FIGURE LEGENDS**

1042

1043

1044 **Figure 1. H3K27ac, H3K27me3, and H3K9me3 levels respond to changes in cell cycle dynamics**

1045

1046 Icons represent the experimentally verified FUCCI cell cycle status in each condition: G2-phase arrest
1047 in *Cdk1-RNAi*-expressing discs, either G1 or G2-phase arrest in *pntP1*-expressing discs, and cell cycle
1048 acceleration in *Dp, E2F1*-overexpressing discs. For better guidance through subsequent figures,
1049 schemes already introduce FUCCI reporter read-outs for phase G1 (green), early S-phase (grey), late
1050 S-phase (red) and G2 (yellow).

1051

1052 **A-D.** Immunostaining for H3K18ac in control **(A)**, *Cdk1-RNAi*-expressing **(B)**, *pntP1*-expressing **(C)** and
1053 *Dp, E2F1*-expressing **(D)** discs. Expression was induced for 24 h in the wing pouch using *rn-GAL4*. The
1054 *rn-GAL4* expressing pouch domain is represented by the tissue above the yellow line (rn^{ts}>). The tissue
1055 below the yellow line represents wild type tissues of the hinge.

1056

1057 **E-T**. Immunostaining for H3K27ac **(E-H)**, H3K4me3 **(I-L)**, H3K27me3 **(M-P)**, H3K9me3 **(Q-T)** in control
1058 **(E,I,M,Q)**, *Cdk1-RNAi*-expressing **(F,J,N,R)**, *pntP1*-expressing **(G,K,O,S)** and *Dp, E2F1*-expressing
1059 **(H,L,P,T)** discs.

1060

1061 **U.** Quantification of relative signal intensities for H3K18ac, H3K27ac, H3K4me3, H3K27me3, and
1062 H3K9me3, presented as pouch-to-hinge ratios (i.e., rn^{ts}-to-wild-type-cell ratio) in *Cdk1-RNAi*-expressing
1063 discs. Mean and 95% CI is shown. Statistical significance was tested using two-tailed Mann-Whitney
1064 test, p value= 0.9591 for H3K18ac (control discs: n=8, *Cdk1-RNAi*-expressing discs: n=8); two-tailed
1065 Unpaired t test, p value=0.0012 for H3K27ac (control discs: n=6, *Cdk1-RNAi*-expressing discs: n=6);
1066 two-tailed Unpaired t test, p value=0.7334 for H3K4me3 (control discs: n=12, *Cdk1-RNAi*-expressing
1067 discs: n=11); two-tailed Unpaired t test, p value<0.0001 for H3K27me3 (control discs: n=9, *Cdk1-RNAi*-
1068 expressing discs: n=9); two-tailed Mann-Whitney test, p value=0.0473 for H3K9me3 (control discs:
1069 n=11, *Cdk1-RNAi*-expressing discs: n=11).

1070

1071 **V.** Quantification of relative signal intensities for H3K18ac, H3K27ac, H3K4me3, H3K27me3, and
1072 H3K9me3, presented as pouch-to-hinge ratios (i.e., rn^{ts}-to-wild-type-cell ratio) in *pntP1*-expressing
1073 discs. Mean and 95% CI is shown. Statistical significance was tested using two-tailed Mann-Whitney
1074 test, p value= 0.5671 for H3K18ac (control discs: n=10, *pntP1*-expressing discs: n=15); two-tailed
1075 Welch's t test, p value=0.0031 for H3K27ac (control discs: n=6, *pntP1*-expressing discs: n=6); two-
1076 tailed Unpaired t test, p value=0.1614 for H3K4me3 (control discs: n=11, *pntP1*-expressing discs:
1077 n=14); two-tailed Unpaired t test, p value<0.0001 for H3K27me3 (control discs: n=9, *pntP1*-expressing
1078 discs: n=9); two-tailed Unpaired t test, p value=0.0002 for H3K9me3 (control discs: n=8, *pntP1*-
1079 expressing discs: n=11).

1080

W. Quantification of relative signal intensities for H3K18ac, H3K27ac, H3K4me3, H3K27me3, and H3K9me3, presented as pouch-to-hinge ratios (i.e., rn^{ts}-to-wild-type-cell ratio) in *Dp, E2F1*-coexpressing discs. Mean and 95% CI is shown. Statistical significance was tested using two-tailed Unpaired t test, p value= 0.0609 for H3K18ac (control discs: n=9, *Dp, E2F1*-coexpressing discs: n=9); two-tailed Unpaired t test, p value=0.0019 for H3K27ac (control discs: n=7, *Dp, E2F1*-coexpressing discs: n=6); two-tailed Unpaired t test, p value=0.4837 for H3K4me3 (control discs: n=12, *Dp, E2F1*-coexpressing discs: n=11); two-tailed Unpaired t test, p value=0.0003 for H3K27me3 (control discs: n=9, *Dp, E2F1*-coexpressing discs: n=9); two-tailed Mann-Whitney test, p value<0.0001 for H3K9me3 (control discs: n=10, *Dp, E2F1*-coexpressing discs: n=10).

Fluorescence intensities are reported as arbitrary units.
Sum projections of multiple confocal sections are shown in **C**, **K**, **M-N**, **O** and **Q-R.**
Maximum projections of multiple confocal sections are shown in **A-B**, **E-F**, **G**, **H**, **I-J**, **P**, **S** and **T**.
Scale bars: 100 µm.
Please refer to **(Fig S1.3A)** for corresponding DAPI images of all discs shown.

Figure 2. Cell cycle-dependent changes in H3K27ac, H3K27me3, and H3K9me3 occur at preexisting genomic sites

---

A-B. Two examples of genomic snapshots of CUT&Tag profiles comparing levels of H3K27ac, H3K27me3 and H3K9me3 in wild type wing discs and in wing discs having expressed *Cdk1*-RNAi for 24 h in the pouch region under the control of rn-GAL4. Tracks for H3K27ac (orange), H3K27me3 (green), and H3K9me3 (red) were normalized against H3 as described in the Materials and Methods and were then visualized using IGV. Black tracks represent the change between control and knockdown conditions computed by subtracting number of sequence reads in *Cdk1-RNAi*-expressing discs from wild type discs for each histone modification. Tracks in **(B)** cover the BX-C Hox gene cluster encoding Ubx, Abd-A and Abd-B targeted by Polycomb silencing.

C-F. Profile plots and heatmaps showing normalized CUT&Tag signals at peaks shared between wild type control and *Cdk1-RNAi*-expressing discs for H3 **(C)**, H3K27ac **(D)**, H3K27me3 **(E)**, and H3K9me3 **(F)** (see Materials and Methods). Averaged and individual signal intensities are centered ±5 kb around the shared peak.

1116 **Figure 3. Developmentally arrested cell populations under physiological conditions exhibit**
1117 **changes in H3K27ac, H3K27me3, and H3K9me3 levels**
1118
1119 **A-C.** Immunostaining for H3K27ac **(A)**, H3K27me3 **(B)**, and H3K9me3 **(C)** in the zone of non-
1120 proliferating cells (ZNC) of developing wing discs. Cells in the ZNC (white brackets) are arrested in
1121 either G1 or G2 phase, and can be identified by the Fly-FUCCI reporter. Among the histone
1122 modifications examined, only H3K27ac, H3K27me3, and H3K9me3 exhibit cell cycle arrest associated
1123 changes in the ZNC.
1124
1125 **D-F.** Immunostaining for H3K27ac **(D)**, H3K27me3 **(E)** and H3K9me3 **(F)** in a hinge cell population
1126 undergoing programmed senescence in developing wing discs.
1127
1128 Discs were stained with DAPI to visualize nuclei.
1129 Scale bars: 50 µm
1130
1131
1132 **Figure 4. Metabolic state sets the rate of H3K27 and H3K9 methylation**
1133
1134 **A-B.** Control wing disc expressing GFP (magenta) for 24 h in the wing pouch domain under the control
1135 of *rn-GAL4* **(A)**. Wing disc expressing GFP and a constitutively active Insulin receptor (*InR-DA*) under
1136 the same conditions **(B)**. GFP expression visualizes the enlarged wing pouch domain in *InR-DA*
1137 expressing discs.
1138
1139 **C.** Quantification of pouch size area in control and *InR-DA*-expressing discs. Mean and 95% CI is
1140 shown. Statistical significance was tested using two-tailed Unpaired t test, p value=0.0432. (control
1141 discs: n=6, *InR-DA*-expressing discs: n=6).
1142
1143 **D-G.** Immunostaining for H3K27me3 in control **(D)**, *InR-DA*-expressing **(E)**, *Cdk1-RNAi*-expressing **(F)**
1144 and *InR-DA, Cdk1-RNAi*-coexpressing **(G)** discs.
1145
1146 **H-K.** Immunostaining for H3K9me3 in control **(H)**, *InR-DA*-expressing **(I)**, *Cdk1-RNAi*-expressing **(J)**
1147 and *InR-DA, Cdk1-RNAi*-coexpressing **(K)** discs.
1148
1149 **L-O.** Immunostaining for H3K4me3 in control **(L)**, *InR-DA*-expressing **(M)**, *Cdk1-RNAi*-expressing **(N)**
1150 and *InR-DA, Cdk1-RNAi*-coexpressing **(O)** discs. Expression was induced for 24 h in the wing pouch
1151 using *rn-GAL4.* Yellow dashed lines indicate the boundary between the wing pouch and hinge regions.
1152 The area above the line corresponds to the *rn-GAL4* expression domain, while the area below
1153 represents wild-type cells.
1154

1155 **P.** Illustration of the dual role of metabolism in regulating histone methylation levels. Metabolism
1156 contributes to the dilution of histone PTMs by accelerating the cell cycle, thereby increasing the
1157 frequency of DNA replication events. Simultaneously, it supports the re-establishment of these PTMs
1158 by supplying essential precursors and cofactors required for methyltransferase activity.
1159
1160 **Q.** Hypothetical model depicting the relationship between histone methylation levels, metabolic rate,
1161 and cell division rate. When metabolic activity and cell division are proportionally coupled (black
1162 diagonal), histone methylation levels are maintained at stable levels. However, when metabolism
1163 outpaces cell division, methylation accumulates.
1164
1165 Discs were stained with DAPI to visualize nuclei.
1166 Sum projections of multiple confocal sections are shown in **A-B.**
1167 Maximum projections of multiple confocal sections are shown in **D-K.**
1168 Scale bars: 100 µm.
1169
1170
1171 **Figure 5. CBP/nejire-mediated H3K27 acetylation peaks during S phase**
1172
1173 **A-B.** Immunostaining for H3K27ac in a control disc expressing the FUCCI reporters *GFP-E2F1*$^{1-230}$
1174 (green) and *mRFP-NLS-CycB*$^{1-266}$ (red) to visualize cell cycle phases **(A).** Magnified region in **(B)** is
1175 demarcated by a white dashed square in **(A).**
1176
1177 **C.** Quantification of normalized H3K27ac intensity level in different cell cycle phases in the pouch region
1178 of control discs. Normalization was performed against the average fluorescence intensity across all cell
1179 cycle phases. Mean and 95% CI is shown. Statistical significance was tested using Repeated Measures
1180 One-Way ANOVA followed by Tukey's post-hoc test for multiple comparison (n=11 discs). Adjusted
1181 $p<0.0001$ for G1 vs. Early S; $p=0.0838$ for G1 vs. Late S; $p<0.0001$ for G1 vs. G2; $p<0.0001$ for Early
1182 S vs. Late S; $p<0.0001$ for Early S vs G2 and $p<0.0001$ for Late S vs G2.
1183
1184 **D-E.** Immunostaining for H3K27ac in control **(D)** and *nejire-RNAi*-expressing **(E)** discs. Expression was
1185 induced for 24 h in the wing pouch using *rn-GAL4.* Yellow dashed lines indicate the boundary between
1186 the wing pouch and hinge regions.
1187
1188 **F-G.** Immunostaining for H3K27ac in control **(F)** and *nejire*-expressing **(G)** discs also expressing the
1189 FUCCI reporters *GFP-E2F1*$^{1-230}$ (green) and *mRFP-NLS-CycB*$^{1-266}$ (red) to visualize cell cycle phases.
1190 Expression of *nejire* was induced for 24 h in the wing pouch using *rn-GAL4.*
1191
1192 **H-I.** Immunostaining for H3K27ac in control **(H)** and *HDAC1-RNAi*-expressing **(I)** discs also expressing
1193 the FUCCI reporters *GFP-E2F1*$^{1-230}$ (green) and *mRFP-NLS-CycB*$^{1-266}$ (red) to visualize cell cycle
1194 phases. Expression of *HDAC1-RNAi* was induced for 24 h in the wing pouch using *rn-GAL4.*

J. Quantification of mean H3K27ac intensity in the pouch region of control or *nejire*-expressing discs. Expression was induced for 24 h in the wing pouch using *rn-GAL4.* Mean and 95% CI is shown. Statistical significance was tested using two-tailed Welch's t test, p value<0.0001. (control discs: n=9, *nejire*-expressing discs: n=9).

J'. Quantification of normalized H3K27ac in G1 phase and Late S phase in the pouch region of control or *nejire*-expressing discs. Expression was induced for 24 h in the wing pouch using *rn-GAL4.* Mean and 95% CI is shown. Statistical significance was tested using Repeated Measures Two-Way ANOVA followed by with Šidák's post hoc test for multiple comparisons (control discs: n=9, *nejire*-expressing discs: n=9). Adjusted p= 0.9482 for Control G1 vs nejire-OE G1; p=0.0064 for Control Late S vs nejire-OE Late S.

K. Quantification of mean H3K27ac intensity in the pouch region of control or *HDAC1-RNAi*-expressing discs. Expression was induced for 24 h in the wing pouch using *rn-GAL4.* Mean and 95% CI is shown. Statistical significance was tested using two-tailed Mann-Whitney test, p value<0.0001. (control discs: n=10, *HDAC1-RNAi*-expressing discs: n=9).

K'. Quantification of normalized H3K27ac intensity level in G1 and Late S phases in the pouch region of control or *HDAC1-RNAi*-expressing discs. Expression was induced for 24 h in the wing pouch using *rn-GAL4.* Mean and 95% CI is shown. Statistical significance was tested using Repeated Measures Two-Way ANOVA followed by with Šidák's post hoc test for multiple comparisons (control discs: n=10, *HDAC1-RNAi*-expressing discs: n=9). Adjusted p= 0.1907 for Control G1 vs HDAC1-RNAi G1; p<0.0001 for Control Late S vs HDAC1-RNAi Late S.

Fluorescence intensities are reported as arbitrary units.
Sum projections of multiple confocal sections are shown in **D-E.**
Scale bars: 100 µm in **A** and **D-E**; 50 µm in **F-G** and **H-I**; 25 µm in **B**.

Figure 6. CBP/Nejire activity and H3K27 acetylation prevent replication stress during S phase

---

A-B. EdU incorporation to visualize DNA replication in the pouch region of control **(A)** and *nejire-RNAi*-expressing **(B)** discs. Dashed yellow squares demarcate magnified regions shown in **(A', B').** Expression was induced for 24 h in the wing pouch using *rn-GAL4.*

C. Quantification of mean EdU intensity per EdU area in the pouch region of control and *nejire-RNAi*-expressing discs, serving as a proxy speed of DNA replication. Mean and 95% CI are shown. Statistical significance was tested using two-tailed Mann Whitney test, p value=0.0001 (control discs: n=11, *nejire-RNAi*-expressing discs: n=11).

1235

1236 **C'.** Quantification of EdU area per DAPI area in the pouch region of control and *nejire-RNAi*-expressing
1237 discs, serving as a proxy number of cells undergoing DNA replication. Mean and 95% CI are shown.
1238 Statistical significance was tested using two-tailed Mann Whitney test, p value<0.0001 (control discs:
1239 n=11, *nejire-RNAi*-expressing discs: n=11).
1240

1241 **D-G.** Immunostaining for γH2Av in control **(F)** and *nejire-RNAi*-expressing **(G)** discs. Expression was
1242 induced for 24 h in the wing pouch using *rn-GAL4.* γH2Av serves as a marker of DNA double strand
1243 breaks. DAPI staining was used to visualize the nuclei in control **(D)** and *nejire-RNAi*-expressing **(E)**
1244 discs. The *rn-GAL4* expression domain is represented by the tissue above the yellow line (rn^{ts}>). The
1245 tissue below the yellow line represents wild type tissues of the hinge.
1246

1247 **H.** Quantification of mean γH2Av intensity in the pouch region of control or *nejire-RNAi*-expressing
1248 discs. Mean and 95% CI are shown. Statistical significance was tested using two-tailed Unpaired t test,
1249 p value=0.0126 (control discs: n=10, *nejire-RNAi*-expressing discs: n=10).
1250

1251 **K.** Immunostaining for H3K27ac (red) and γH2Av (cyan) in wing imaginal discs with clones of Δ*HisC*
1252 mutant clones deleting the histone cluster and rescued by a *12×His-GU*$^{H3\text{-}K27R}$ transgene.
1253

1254 **L.** Illustration of the role of CBP/nej and HDAC1 in modulating levels of H3K27ac during S-phase to
1255 prevent replication stress
1256

1257 Discs were stained with DAPI to visualize nuclei.
1258 Fluorescence intensities are reported as arbitrary units.
1259 Sum projections of multiple confocal sections are shown in **A-B** and **D-G.**
1260 Maximum projections of multiple confocal sections are shown in **K.**
1261 Scale bars: 100 μm in **A-B**, **D-G**, **I-J** and **K.**
1262

1263 **SUPPLEMENTARY FIGURE LEGENDS**

1264

1265 **Figure S1.1. Cell cycle manipulation models for assessing histone modification dynamics**

1266

1267 **A.** A control wing disc after 24 h of *UAS-GFP*-expression in the pouch, under the control of the *rn-GAL4*
1268 (*rotund-GAL4*) driver. GFP-expression visualizes the tissue domain subject to manipulation throughout
1269 this study (magenta).

1270

1271 **B.** Schematic representation of the Fly-FUCCI cell cycle reporter system, utilizing the degradable *GFP-*
1272 *E2F1*$^{1-230}$ (green) and *mRFP-NLS-CycB*$^{1-266}$ (red) as sensors to visualize cell cycle phases. Individual
1273 fluorophore expression indicates cells in G1 or late S-phase, respectively. Combined expression of both
1274 GFP and RFP labels cells is observed in early and late G2. Cells in late mitosis and early S-phase lack
1275 expression of either GFP or RFP. Cells in early S-phase are specifically detected by EdU incorporation
1276 (Crucianelli et al., 2022; Zielke et al., 2014). Cells in mitosis are positioned in very apical positions of
1277 the tissue and are not represented in our study.

1278

1279 **C-G.** Cell cycle dynamics in control discs **(C, E)** and discs expressing *Cdk1-RNAi* for 24 h under the
1280 control of *rn-GAL4* **(D, F)**. FUCCI reporters *GFP-E2F1*$^{1-230}$ (green) and *mRFP-NLS-CycB*$^{1-266}$ (red) were
1281 used to visualize cell cycle phases **(C, D)** and EdU incorporation was used to detect DNA replication in
1282 S-phase cells **(E, F).** Cdk1 knockdown in the wing pouch domain leads to a cell cycle phase shift toward
1283 G2 phase **(D)**, and a corresponding loss of EdU incorporation **(F)** combined demonstrating a
1284 pronounced arrest in G2. **(G)** Quantification of mean EdU intensity per DAPI area in the pouch region
1285 of control and *Cdk1-RNAi*-expressing discs, serving as a proxy for relative DNA replication activity.
1286 Mean and 95% CI are shown. Statistical significance was tested using two-tailed Welch's test, p value
1287 <0.0001 (control discs: n=11, *Cdk1-RNAi*-expressing discs: n=12).

1288

1289 **H-L.** Cell cycle dynamics in control discs **(H, J)** and discs expressing *pntP1* **(I, K)** for 24 h under the
1290 control of *rn-GAL4.* FUCCI reporters *GFP-E2F1*$^{1-230}$ (green) and *mRFP-NLS-CycB*$^{1-266}$ (red) were used
1291 to visualize cell cycle phases **(H, I)** and EdU incorporation was used to detect DNA replication in S-
1292 phase cells **(J, K).** Pointed-P1 overexpression in the wing pouch domain leads to a cell cycle phase
1293 shift towards either the G1 or the G2 phase **(I)**, correlating with a loss of EdU incorporation **(K)**.
1294 Combined, this demonstrates a pronounced arrest in either G1 or G2. Mechanistically, the choice for
1295 either cell cycle phase is not known. **(L)** Quantification of mean EdU intensity per DAPI area in the
1296 pouch region of control and *pntP1*-expressing discs, serving as a proxy for relative DNA replication
1297 activity. Mean and 95% CI is shown. Statistical significance was tested using two-tailed Mann-Whitney
1298 test, p value=0.0043 (control discs: n=6, *pntP1*-expressing discs: n=6).

1299

1300 **M-Q.** Cell cycle dynamics in control discs **(M, O)** and discs expressing *Dp, E2F1* **(N, P)** for 24 h under
1301 the control of *rn-GAL4.* FUCCI reporters *GFP-E2F1*$^{1-230}$ (green) and *mRFP-NLS-CycB*$^{1-266}$ (red) were
1302 used to visualize cell cycle phases **(M, N)** and EdU incorporation was used to detect DNA replication in

1303 S-phase cells **(O,P).** dDp and dE2F1 co-expression in the wing pouch domain reduces the number of
1304 cells in either G1 or G2 **(N)**, and an increase in S-phase cells as well as an elevation of EdU
1305 incorporation **(P)** in the wing pouch region, confirming frequent entry and rapid progression through the
1306 cell cycle. **(Q)** Quantification of mean EdU intensity per DAPI area in the pouch region of control and
1307 *Dp, E2F1*-coexpressing discs, serving as a proxy for relative DNA replication activity. Mean and 95%
1308 CI is shown. Statistical significance was tested using two-tailed Welch's t test, p value=0.0069 (control
1309 discs: n=6, *Dp, E2F1*-expressing discs: n=5).
1310
1311 Discs were stained with DAPI to visualize nuclei.
1312 Fluorescence intensities are reported as arbitrary units.
1313 Yellow dashed lines represent the pouch region of wing discs.
1314 Sum projections of multiple confocal sections are shown in **A, E-F, J-K, M-N** and **O-P.**
1315 Maximum projections of multiple confocal sections are shown in **C-D** and **H-I.**
1316 Scale bars: 100 µm.
1317
1318
1319 **Figure S1.2. Histone modifications are largely insensitive to cell cycle manipulations**
1320
1321 **A-D.** Immunostaining for H3K9ac in control **(A)**, *Cdk1-RNAi*-expressing **(B)**, *pntP1*-expressing **(C)** and
1322 *Dp, E2F1*-expressing **(D)** discs. Expression was induced for 24 h in the wing pouch using *rn-GAL4*. The
1323 *rn-GAL4* expression pouch domain is represented by the tissue above the yellow line (rn^{ts}>). The tissue
1324 below the yellow line represents wild type tissues of the hinge. Icons represent the experimentally
1325 verified FUCCI cell cycle status (see **Fig S1.1**) in each condition: G2-phase arrest in *Cdk1-RNAi*-
1326 expressing discs **(B)**, combined G1 and G2-phase arrest in *pntP1*-expressing discs **(C)**, and cell cycle
1327 acceleration in *Dp, E2F1*-coexpressing discs **(D)**.
1328
1329 **E-H**. Immunostaining for H4K8ac in control **(E)**, *Cdk1-RNAi*-expressing **(F)**, *pntP1*-expressing **(G)** and
1330 *Dp, E2F1*-coexpressing **(H)** discs.
1331
1332 **I-L.** Immunostaining for total acetylated lysines in control **(I)**, *Cdk1-RNAi*-expressing **(J)**, *pntP1*-
1333 expressing **(K)** and *Dp, E2F1*-coexpressing **(L)** discs.
1334
1335 **M-P.** Immunostaining for H3K18crotonylation in control **(M)**, *Cdk1-RNAi*-expressing **(N)**, *pntP1*-
1336 expressing **(O)** and *Dp, E2F1*-coexpressing **(P)** discs.
1337
1338 **Q-T.** Immunostaining for total H3K9me1/2/3 methylation in control **(I)**, *Cdk1-RNAi*-expressing **(J)**,
1339 *pntP1*-expressing **(K)** and *Dp, E2F1*-coexpressing **(L)** discs.
1340
1341 **U.** Quantification of relative signal intensities for H3K9ac, H4K8ac, total acetylated lysine,
1342 H3K18crotonylation, and H3K9me1/2/3, presented as pouch-to-hinge ratios (rn^{ts}-to-wild-type-cell ratio)

in *Cdk1-RNAi*-expressing discs. Mean and 95% CI is shown. Statistical significance was tested using two-tailed Unpaired t test, p value= 0.4268 for H3K9ac (control discs: n=5, *Cdk1-RNAi*-expressing discs: n=5); two-tailed Unpaired t test, p value=0.8936 for H4K8ac (control discs: n=5, *Cdk1-RNAi*-expressing discs: n=5); two-tailed Unpaired t test, p value=0.5553 for total acetylated lysines (control discs: n=6, *Cdk1-RNAi*-expressing discs: n=6); two-tailed Mann-Whitney test, p value=0.4779 for H3K18crot (control discs: n=11, *Cdk1-RNAi*-expressing discs: n=11); two-tailed Unpaired t test, p value=0.9619 for H3K9me1/2/3 (control discs: n=9, *Cdk1-RNAi*-expressing discs: n=10).

V. Quantification of relative signal intensities for H3K9ac, H4K8ac, total acetylated lysine, H3K18crotonylation, and H3K9me1/2/3, presented as pouch-to-hinge ratios (rn^{ts}-to-wild-type-cell ratio) in *pntP1*-expressing discs. Mean and 95% CI is shown. Statistical significance was tested using two-tailed Unpaired t test, p value= 0.1975 for H3K9ac (control discs: n=8, *pntP1*-expressing discs: n=10); two-tailed Unpaired t test, p value=0.2752 for H4K8ac (control discs: n=12, *pntP1*-expressing discs: n=12); two-tailed Unpaired t test, p value=0.0012 for total acetylated lysines (control discs: n=6, *pntP1*-expressing discs: n=6); two-tailed Unpaired t test, p value=0.6621 for H3K18crot (control discs: n=7, *pntP1*-expressing discs: n=7); two-tailed Mann-Whitney test, p value=0.2403 for H3K9me1/2/3 (control discs: n=6, *pntP1*-expressing discs: n=6).

W. Quantification of relative signal intensities for H3K9ac, H4K8ac, total acetylated lysine, H3K18crotonylation, and H3K9me1/2/3, presented as pouch-to-hinge ratios (rn^{ts}-to-wild-type-cell ratio) in *Dp, E2F1*-coexpressing discs. Mean and 95% CI is shown. Statistical significance was tested using two-tailed Unpaired t test, p value= 0.0282 for H3K9ac (control discs: n=8, *Dp, E2F1*-coexpressing discs: n=8); two-tailed Mann-Whitney test, p value=0.0759 for H4K8ac (control discs: n=11, *Dp, E2F1*-coexpressing discs: n=11); two-tailed Mann-Whitney test, p value=0.2403 for total acetylated lysines (control discs: n=6, *Dp, E2F1*-coexpressing discs: n=6); two-tailed Mann-Whitney test, p value=0.0728 for H3K18crot (control discs: n=7, *Dp, E2F1*-coexpressing discs: n=7); two-tailed Unpaired t test, p value=0.0154 for H3K9me1/2/3 (control discs: n=10, *Dp, E2F1*-coexpressing discs: n=10).

Fluorescence intensities are reported as arbitrary units.
Sum projections of multiple confocal sections are shown in **C-T.**
Scale bars: 100 µm.
Please refer to **(Fig S1.3B)** for corresponding DAPI images of all discs shown.

Figure S1.3 Corresponding DAPI images for Fig 1 and Fig S1.2

Representation of DAPI images matched to the images of histone modifications in control, *Cdk1-RNAi*-expressing, *pntP1*-expressing and *Dp, E2F1*-coexpressing wing discs shown in Fig 1 and Fig S1.2.

Discs were stained with DAPI to visualize nuclei.
Sum and max projections of multiple confocal sections are shown.

Scale bars: 100 µm.

Figure S2.1. Comparative analysis of Histone H3 and H3K27ac, H3K27me3, and H3K9me3 histone modifications by CUT&Tag in control and Cdk1 RNAi- expressing discs

---

A-D. MA plots displaying differential enrichment of histone modifications analysed by by CUT&Tag for H3, H3K27ac, H3K27me3, and H3K9me3 (in rows). Each point represents a shared or unique genomic peak identified by our analysis in control and Cdk1-RNAi expressing discs (shared peaks **(A)**, unique peaks in control **(B)**, unique peaks in cdk1-RNAi **(C)**), or a 500 bp genomic fragment not called as any peak in our analysis (other genomic regions **(D)**). The x-axis displays the mean normalized read count on a log10 scale, representing an average signal intensity across samples or conditions. The y-axis displays the log2 fold change (log2 ratio of read counts) between the Cdk1-RNAi and control conditions, reflecting the magnitude and direction of differential enrichment. Peaks are color-coded by modification type: blue for H3, orange for H3K27ac, green for H3K27me3, and red for H3K9me3. Regions with an adjusted p-value<0.1 are colored accordingly, highlighting statistically significant differential peaks; non-significant peaks (ns, adjusted p-value ≥0.1) are shown in gray.

E. Each subplot depicts the distribution of log2 fold change values (Cdk1-RNAi compared to control) for genomic regions categorized as Shared (peaks detected in both conditions), Control-Unique (peaks specific to control), Cdk1-RNAi-Unique (peaks specific to Cdk1-RNAi expressing discs), and Other (genomic fragments of 500bp not included in any called peaks). The x-axis indicates these categorical groups, and the y-axis shows the log2 fold change of normalized counts between Cdk1-RNAi and control samples. Each point represents an individual genomic region, colored by histone mark: blue (H3), orange (H3K27ac), green (H3K27me3), and red (H3K9me3). Black horizontal bars indicate the mean log2 fold change within each group. Peaks are color-coded by modification type: blue for H3, orange for H3K27ac, green for H3K27me3, and red for H3K9me3. Regions with an adjusted p-value<0.1 are colored accordingly, highlighting statistically significant differential peaks; non-significant peaks (ns, adjusted p-value ≥0.1) are shown in gray.

Figure S2.2. Cell cycle–dependent fluctuations of H3K27ac and H3K27me3 are not due to competitive residue occupancy

---

A-B. H3K27me3 staining in control **(A)** or *E(z)-RNAi*-expressing **(B)** discs. Knockdown of the H3K27me3 writer E(z) causes a reduction in H3K27me3 level in the pouch of the wing disc.

C-D. H3K27ac staining in control **(C)** or *E(z)-RNAi*-expressing **(D)** discs. Knockdown of the H3K27me writer E(z) causes no corresponding increase in H3K27ac level.

1423 **E-F.** H3K27ac staining in control **(E)** and *nejire-RNAi*-expressing **(F)** discs. Knockdown of the H3K27ac
1424 writer CBP/nej causes a reduction of H3K27ac level in the pouch of the wing disc.
1425
1426 **G-H.** H3K27me3 staining in control **(G)** and *nejire-RNAi*-expressing **(H)** discs. Knockdown of the
1427 H3K27ac writer CBP/nej causes no corresponding increase in H3K27me3 level.
1428
1429 Discs were stained with DAPI to visualize nuclei.
1430 Maximum projections of multiple confocal sections are shown in **A-B.**
1431 Sum projections of multiple confocal sections are shown in **C-D, E-F** and **G-H.**
1432 Scale bars: 100 μm.
1433
1434
1435 **Figure S3.1. Visualization of cell cycle-arrested cell populations and histone modifications in**
1436 **developing wing imaginal disc**
1437
1438 **A.** Schematic representation of the zone of non-proliferation cells (ZNC) (adapted from (Johnston and
1439 Edgar, 1998)).
1440
1441 **B-C.** The Fly-FUCCI system and EdU incorporation assay were used to visualize the spatial pattern of
1442 cell cycle arrest within the ZNC. In the anterior ZNC, central margin cells arrest in G1 phase, while
1443 adjacent cells arrest in G2. Cells in the posterior ZNC uniformly arrest in G1. The entire ZNC region
1444 also lacks EdU incorporation, indicating absence of S-phase entry. White arrowheads indicate the ZNC.
1445
1446 **D.** Elevated SA-β-gal activity marks two clusters of cell cycle–arrested cells undergoing programmed
1447 senescence (indicated by yellow arrowheads) in developing wing discs.
1448
1449 **E,F.** Immunostaining for H3K18ac **(E)** and H3K4me3 **(F)** in the zone of non-proliferation cells (ZNC) of
1450 developing wing discs. Neither histone modification shows detectable changes in this region.
1451
1452 **G,H.** Immunostaining for H3K18ac **(G)** and H3K4me3 **(H)** in senescent cell populations of the hinge in
1453 developing wing discs. Neither histone modification shows detectable changes in this region.
1454
1455 Discs were stained with DAPI to visualize nuclei.
1456 Maximum projection of multiple confocal sections is shown in **C.**
1457 Sum projections of multiple confocal sections are shown in **A-B and D.**
1458 Scale bars: 100 μm in **B-D**; 50 μm in **E-H.**
1459
1460
1461 **Figure S3.2. Polycomb target gene expression remains stable despite altered cell cycle**
1462 **dynamics**

A-L. Immunostaining for proteins expressed by Polycomb target genes: Cut **(A, B),** Engrailed/invected **(C, D),** Nubbin **(E, F),** Antennapedia **(G, H),** Patched **(I, J)** and Wingless **(K, L)** in control **(A, C, E, G, I, K)** and *Cdk1-RNAi*-expressing **(B, D, F, H, J, L)** wing discs.

M-R. Immunostaining for proteins expressed by Polycomb target genes: Antennapedia **(M, N),** Engrailed/i**nvected (O, P)** and Patched **(Q, R)** in control **(M, O, Q)** and *Dp, E2F1*-coexpressing **(N, P, R)** wing discs.

S. A control wing disc after 24 h of *UAS-GFP*-expression in the pouch (magenta), under the control of the *rn-GAL4* (*rotund-GAL4*) driver, displayed to reference the manipulated pouch domain in Figures A-R. Please note that this is the same disc shown in **Fig S1.1 A**.

Discs were stained with DAPI to visualize nuclei.
Sum projections of multiple confocal sections are shown in **A-S.**
Scale bars: 100 µm.

Figure S4.1. Increased insulin signaling promotes faster proliferation and growth independent of changes to the distribution of cell cycle phases

---

A-B. Protein synthesis visualized by OPP incorporation in control **(A)** and *InR-DA*-expressing **(B)** discs. Yellow dashed lines indicate the boundary between the wing pouch and hinge regions. The area above the line corresponds to the *rn-GAL4* expression domain, while the area below represents wild-type cells. The *InR-DA*-expressing wing pouch exhibits higher rates of protein synthesis, reflecting an increased biosynthetic capacity promoted by higher InR/PI3K/Akt activity.

C. Quantification of mean OPP intensity in the pouch region of control and *InR-DA*-expressing discs. Mean and 95% CI is shown. Statistical significance was tested using two-tailed Unpaired t test, p value<0.0001. (control discs: n=5, *InR-DA*-expressing discs: n=6).

D-E. EdU incorporation visualizes DNA replication in the pouch region of control **(D)** and *InR-DA*-expressing **(E)** discs. Dashed yellow squares highlight the magnified regions shown in **(D',E')**. *InR-DA*-expressing wing pouch shows higher levels of EdU intensities, reflecting accelerated speed of DNA replication. Rates of EdU incorporation in *InR-DA*-expressing discs were previously reported and quantified (Crucianelli et al., 2022).

F-G. Cell cycle dynamics in control **(F)** and *InR-DA*-expressing **(G)** discs. FUCCI reporters *GFP-E2F1*$^{1-230}$ (green) and *mRFP-NLS-CycB*$^{1-266}$ (red) were used to visualize cell cycle phases. Note that

expression of a constitutively active Insulin receptor does not alter the cell cycle phase profile of the wing pouch compared to control disc.

Discs were stained with DAPI to visualize nuclei.
Fluorescence intensities are reported as arbitrary units.
Maximum projections of multiple confocal sections are shown in **F-G.**
Sum projections of multiple confocal sections are shown in **A-B** and **D-E.**
Scale bars: 100 µm in **A,B**, **D,E**, **F,G;** 50 µm in zoomed-in **D,E.**

Figure S4.2. Persistence methyltransferase activity drives H3K9me3 accumulation through metabolic changes coupled to a senescent cell cycle arrest

---

A-B. Senescence-associated β-galactosidase (SA-β-gal) activity (cyan or gray) in control **(A)** and *egr*-expressing **(B)** discs. TRE-RFP reporter (magenta) visualizes JNK-pathway activity. SA-β-gal activity in *egr*-expressing discs was previously reported and quantified (Jaiswal et al., 2023).

C-D. EdU incorporation (gray or cyan) visualizes DNA replication in control (B) and *egr*-expressing (D) discs. TRE-RFP reporter (magenta) visualizes JNK-pathway activity. EdU incorporation was previously reported and quantified (Jaiswal et al., 2023, Floc'hlay et al., 2023) .

E-F. Cell cycle dynamics in control **(E)** and *egr*-expressing **(F)** discs. FUCCI reporters *GFP-E2F1*$^{1-230}$ (green) and *mRFP-NLS-CycB*$^{1-266}$ (red) were used to visualize cell cycle phases.

G. A model illustrating inflammatory tissue damage in *Drosophila* wing imaginal discs. Eiger expression activates the JNK pathway, an early stress response, which induces a senescence-like cell-cycle arrest in the G2 phase at center of the tissue damage and triggers a senescence program (Cosolo et al., 2019). These arrested cells secrete Unpaired cytokines, which activate the JAK/STAT pathway in surrounding cells, promoting compensatory proliferation during tissue regeneration (Crucianelli et al., 2022; Floc'hlay et al., 2023; Herrera & Bach, 2019; Jaiswal et al., 2023; La Fortezza et al., 2016; Santabarbara-Ruiz et al., 2015; Worley et al., 2022). At the periphery of the damage site, cells remain in a quiescent state (Maya et al., 2024).

H-I. Immunostaining for H3K9me3 in *egr*-expressing disc **(H).** The magenta frame highlights G2-arrested senescent cells, which show elevated H3K9me3 levels. The cyan frame marks cells undergoing compensatory proliferation, where H3K9me3 levels are reduced. The yellow frame indicates quiescent cells, which have higher H3K9me3 levels than proliferating cells **(I).**

Discs were stained with DAPI to visualize nuclei.
Maximum projections of multiple confocal sections are shown in **H.**

1542 Sum projections of multiple confocal sections are shown in **A-D** and **E-F.**
1543 Scale bars: 100 µm in **A-B**, **C-D**, **E-F** and **H**; 10 µm in **I**.
1544
1545
1546 **Figure S5.1. Total H3 and acetyl-lysine dynamics do not recapitulate the S phase-associated**
1547 **increase in H3K27ac**

1548
1549 **A-B.** Immunostaining for H3 in a developing control disc **(A**), with a magnified region (demarcated by a
1550 white dashed square) shown in panel B, also expressing the FUCCI reporter (*GFP-E2F1*$^{1-230}$ (green)
1551 and *mRFP-NLS-CycB*$^{1-266}$ (red)) to visualize cell cycle phases.
1552
1553 **C.** Quantification of normalized H3 intensity level with respect to different cell cycle phases in the pouch
1554 region of control discs. Please note that normalization was performed against the average fluorescence
1555 intensity across all cell cycle phases. Mean and 95% CI is shown. Statistical significance was tested
1556 using Repeated Measures One-Way ANOVA followed by Tukey's post-hoc test for multiple comparison
1557 (n=11 discs). Adjusted p= 0.0192 for G1 vs. Early S; p<0.0001 for G1 vs. Late S; p<0.0001 for G1 vs.
1558 G2; p<0.0001 for Early S vs. Late S; p<0.0001 for Early S vs G2 and p=0.4147 for Late S vs G2.
1559
1560 **D-E.** Immunostaining for total acetylated lysine level in a developing control disc **(D),** with a magnified
1561 region (demarcated by a white dashed square) in panel E, also expressing the FUCCI reporters (*GFP-*
1562 *E2F1*$^{1-230}$ (green) and *mRFP-NLS-CycB*$^{1-266}$ (red)) to visualize cell cycle phases.
1563
1564 **F.** Quantification of normalized total acetylated lysine level in different cell cycle phases in the pouch
1565 region of control discs. Please note that normalization was performed against the average fluorescence
1566 intensity across all cell cycle phases. Mean and 95% CI is shown. Statistical significance was tested
1567 using Repeated Measures One-Way ANOVA followed by Tukey's post-hoc test for multiple comparison
1568 (n=13 discs). Adjusted p<0.0001 for G1 vs. Early S; p<0.0001 for G1 vs. Late S; p<0.0001 for G1 vs.
1569 G2; p<0.0001 for Early S vs. Late S; p<0.0001 for Early S vs G2 and p<0.0001 for Late S vs G2.
1570
1571 **G-H.** Immunostaining for H3K27ac in control **(G)** and *nejire*-expressing **(H)** discs, also expressing the
1572 FUCCI reporters (*GFP-E2F1*$^{1-230}$ (green) and *mRFP-NLS-CycB*$^{1-266}$ (red)) to visualize cell cycle phases.
1573 The location of magnified regions shown in Main Figure 5F and G is indicated by white dashed squares.
1574
1575 **I-J.** Immunostaining for H3K27ac in control **(I)** and *HDAC1-RNAi*-expressing **(J)** discs also expressing
1576 the FUCCI reporters (*GFP-E2F1*$^{1-230}$ (green) and *mRFP-NLS-CycB*$^{1-266}$ (red)) to visualize cell cycle
1577 phases. The location of magnified regions shown in Main Figure 5H and I is indicated by white dashed
1578 squares.
1579
1580 Fluorescence intensities are reported as arbitrary units.
1581 Maximum projections of multiple confocal sections are shown in **D-E.**

1582 Scale bars: 100 µm.
1583
1584
1585 **Figure S5.2. Total H3K18ac and H4K8ac dynamics only partially recapitulate the S phase-**
1586 **associated increase in H3K27ac**
1587
1588 **A-B.** Immunostaining for H3K18ac in a developing control disc **(A),** with a magnified region (demarcated
1589 by a white dashed square) in panel B, in the background of FUCCI reporters (*GFP-E2F1*$^{1-230}$ (green)
1590 and *mRFP-NLS-CycB*$^{1-266}$ (red)) to visualize cell cycle phases.
1591
1592 **C.** Quantification of normalized H3K18ac intensity level in different cell cycle phases in the pouch region
1593 of control discs. Please note that normalization was performed against the average fluorescence
1594 intensity across all cell cycle phases. Mean and 95% CI is shown. Statistical significance was tested
1595 using Repeated Measures One-Way ANOVA followed by Tukey's post-hoc test for multiple comparison
1596 (n=13 discs). Adjusted p=0.0003 for G1 vs. Early S; p<0.0001 for G1 vs. Late S; p<0.0001 for G1 vs.
1597 G2; p<0.0001 for Early S vs. Late S; p<0.0001 for Early S vs G2 and p=0.0042 for Late S vs G2.
1598
1599 **D-E.** Immunostaining for H4K8ac in a normally developing control disc **(D),** with a magnified region
1600 (demarcated by a white dashed square) in panel E, also expressing the FUCCI reporters (*GFP-E2F1*$^{1-}$
1601 ^{230} (green) and *mRFP-NLS-CycB*$^{1-266}$ (red)) to visualize cell cycle phases.
1602
1603 **F.** Quantification of normalized H4K8ac intensity level in different cell cycle phases in the pouch region
1604 of control discs. Please note that normalization was performed against the average fluorescence
1605 intensity across all cell cycle phases. Mean and 95% CI is shown. Statistical significance was tested
1606 using Repeated Measures One-Way ANOVA followed by Tukey's post-hoc test for multiple comparison
1607 (n=12 discs). Adjusted p=0.0018 for G1 vs. Early S; p<0.0001 for G1 vs. Late S; p<0.0001 for G1 vs.
1608 G2; p<0.0001 for Early S vs. Late S; p<0.0001 for Early S vs G2 and p=0.1076 for Late S vs G2.
1609
1610 **G-H.** Immunostaining for H3K27ac in control **(G)** and *nejire-RNAi*-expressing **(H)** discs. Same disc is
1611 also shown in Figure 5D and E but repeated here to allow for direct comparison with **(I-N)**.
1612
1613 **I-J.** Immunostaining for H3K18ac in control **(I)** and *nejire-RNAi*-expressing **(J)** discs.
1614
1615 **K-L.** Immunostaining for H4K8ac in control **(K)** and *nejire-RNAi*-expressing **(L)** discs.
1616
1617 **M-N.** Immunostaining for H3K18crot in control **(M)** and *nejire-RNAi*-expressing **(N)** discs. Yellow dashed
1618 lines indicate the boundary between the wing pouch and hinge regions.
1619
1620 **O.** Expression of a Crisper-tagged CBP/nej-GFP (Marsh et al., 2025) in a developing disc.
1621

1622 Discs were stained with DAPI to visualize nuclei.
1623 Fluorescence intensities are reported as arbitrary units.
1624 Maximum projections of multiple confocal sections are shown in **A-B** and **D-E.**
1625 Sum projections of multiple confocal sections are shown in **G-H, I-J, K-L** and **M-N.**
1626 Scale bars: 100 μm
1627
1628
1629 **Figure S6. CBP/nej and H3K27ac are required to prevent replication stress**
1630
1631 **A-C.** Expression of the JNK pathway reporter TRE-RFP in control (A), *nejire-RNAi*-expressing (B) and
1632 *bsk^{DN}, nejire-RNAi*-coexpressing (C) discs.
1633
1634 **D.** Cell cycle dynamics in *bsk^{DN}, nejire-RNAi*-coexpressing (D) disc. FUCCI reporters *GFP-E2F1$^{1-230}$*
1635 (green) and *mRFP-NLS-CycB$^{1-266}$* (red) were used to visualize cell cycle phases. Even when JNK
1636 pathway activity is suppressed, one can still observe a shift of cells to the G2 phase of the cell cycle
1637 *nejire-RNAi*-expressing discs.
1638
1639 **E-F.** EdU incorporation to visualize DNA replication in the pouch region of control (E) and *nejire*-
1640 expressing (F) discs.
1641
1642 **G.** Quantification of mean EdU intensity per EdU area in the pouch region of control and *nejire*-
1643 expressing discs, serving as a proxy for speed of DNA replication. Mean and 95% CI are shown.
1644 Statistical significance was tested using two-tailed Mann Whitney test, p value=0.5737 (control discs:
1645 n=8, *nejire*-expressing discs: n=8).
1646
1647 **G'.** Quantification of EdU area per DAPI area in the pouch region of control and *nejire*-expressing discs,
1648 serving as a proxy number of cells undergoing DNA replication. Mean and 95% CI are shown. Statistical
1649 significance was tested using a two-tailed Mann Whitney test, p value=0.2345 (control discs: n=8, *nejire*-
1650 expressing discs: n=8).
1651
1652 **H-I.** Immunostaining for Abd-B in control discs **(H)** and in discs expressing *12×His-GU$^{H3-K27R}$* transgenes
1653 and containing clones homozygous mutant for a deletion of the histone gene cluster Δ*HisC* **(I)**.
1654
1655 Discs were stained with DAPI to visualize nuclei.
1656 Fluorescence intensities are reported as arbitrary units.
1657 Sum projections of multiple confocal sections are shown in **A-C**, **E-F** and **H-I**.
1658 Scale bars: 100 μm.
1659
1660
1661

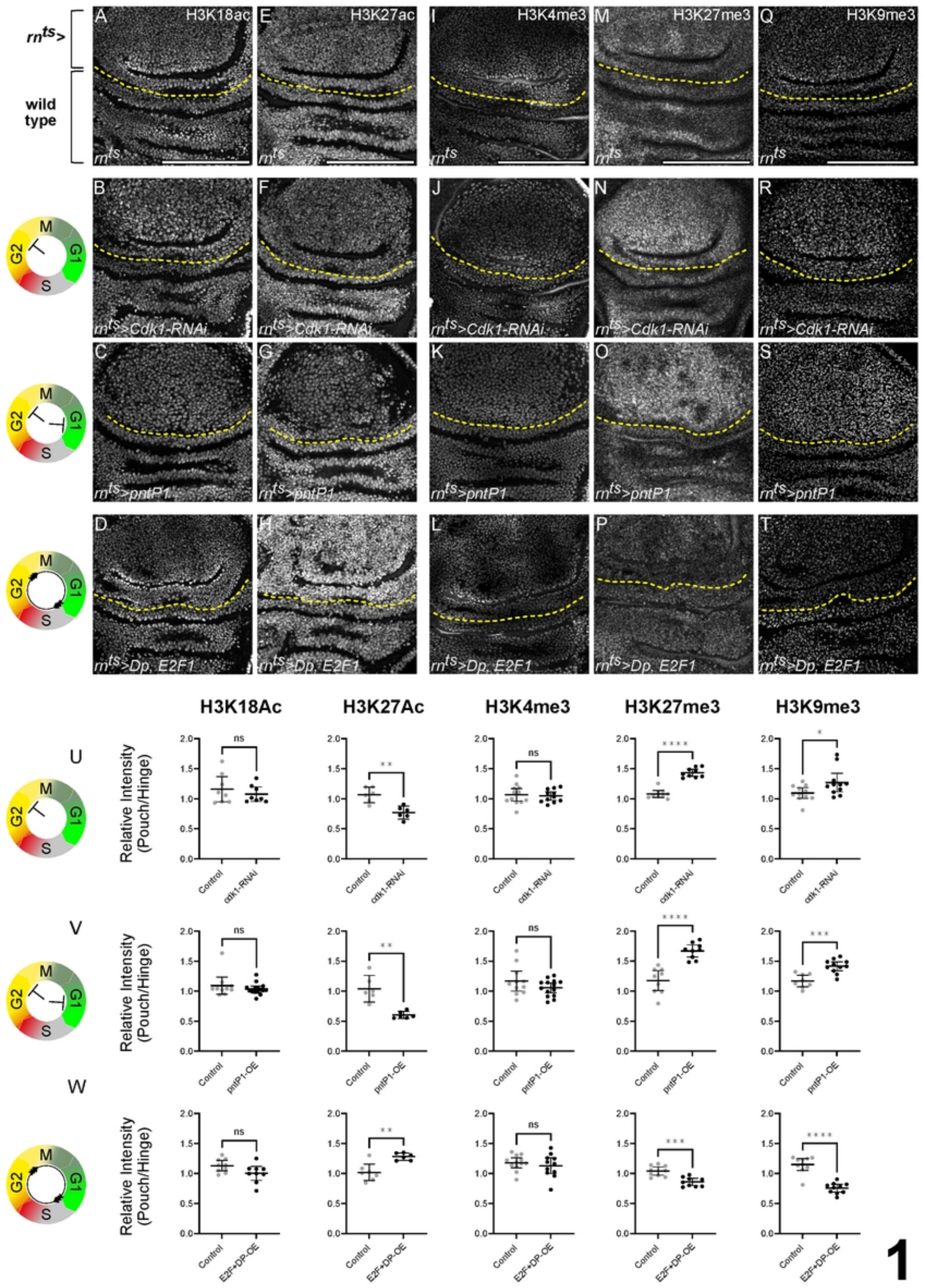

1

Main Figure 1

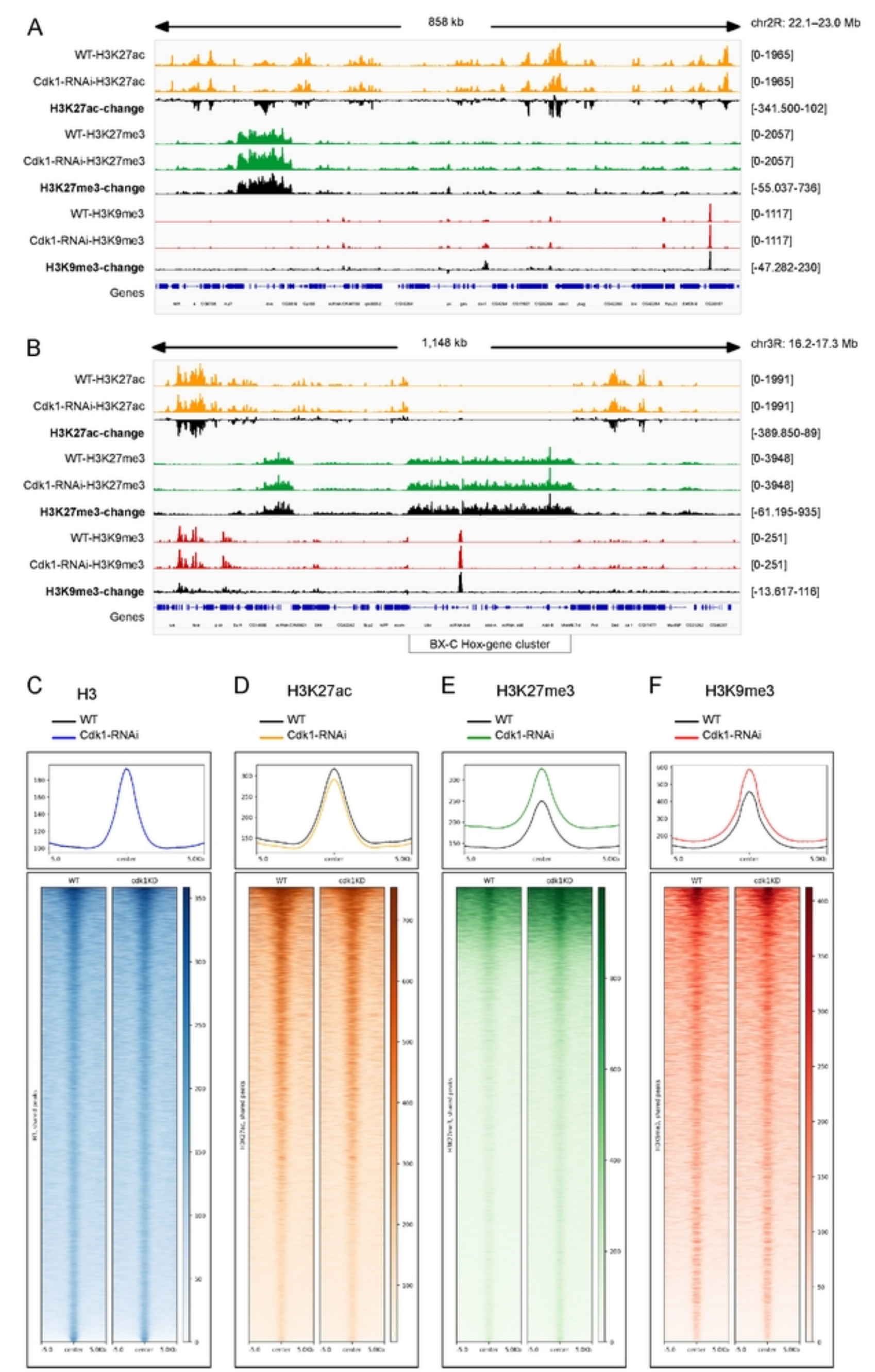

2

Main Figure 2

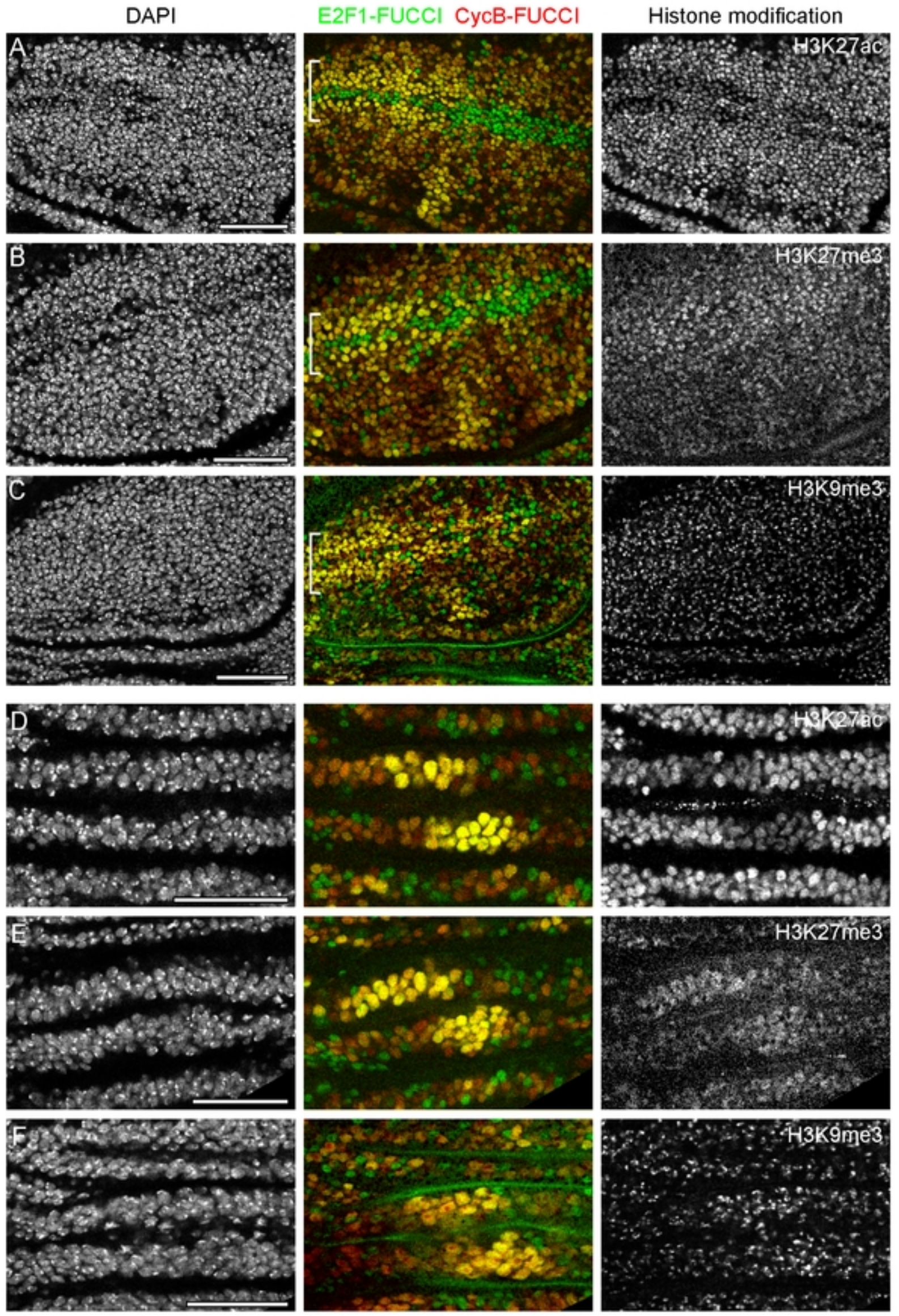

3

Main Figure 3

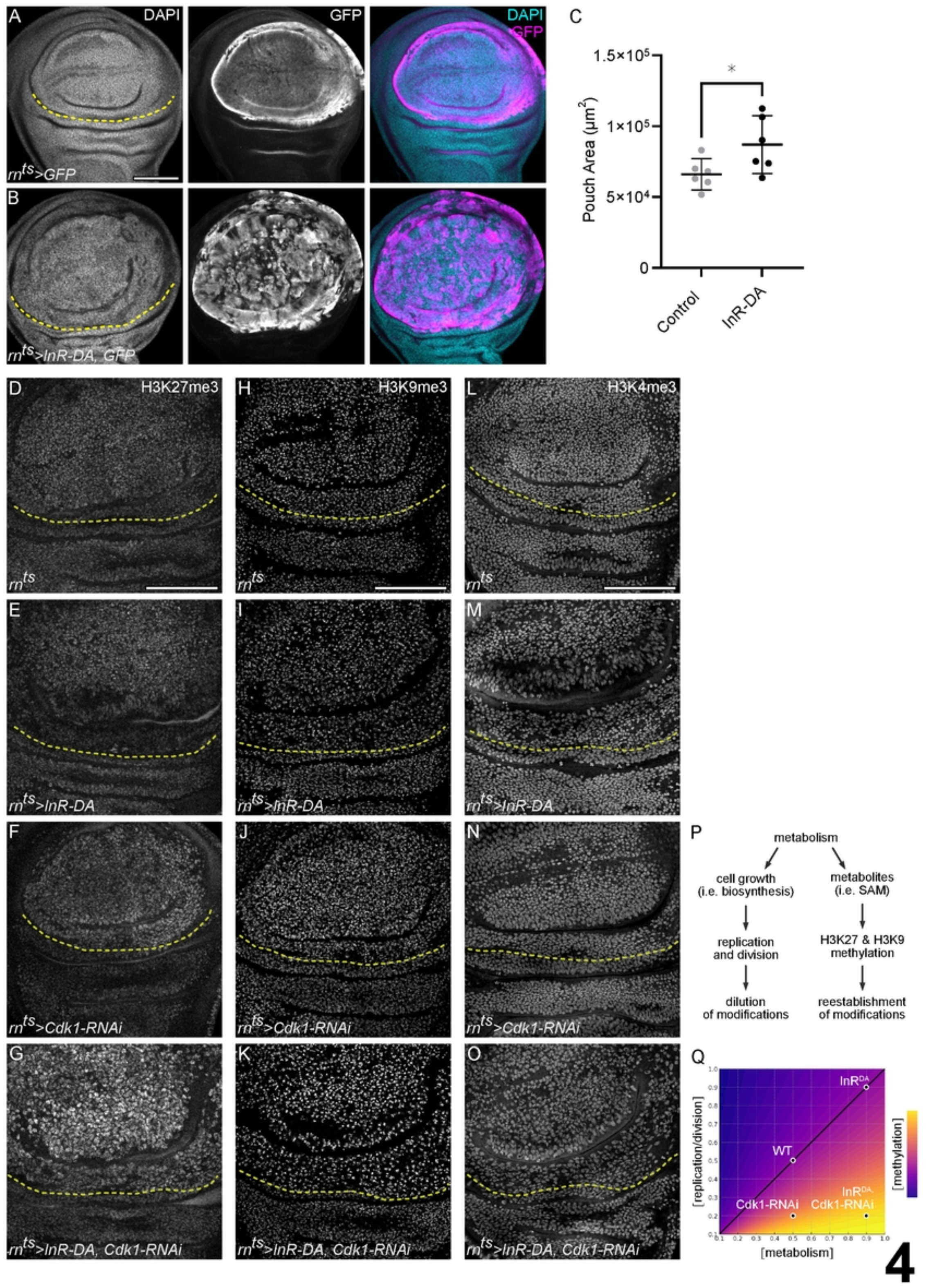

Main Figure 4

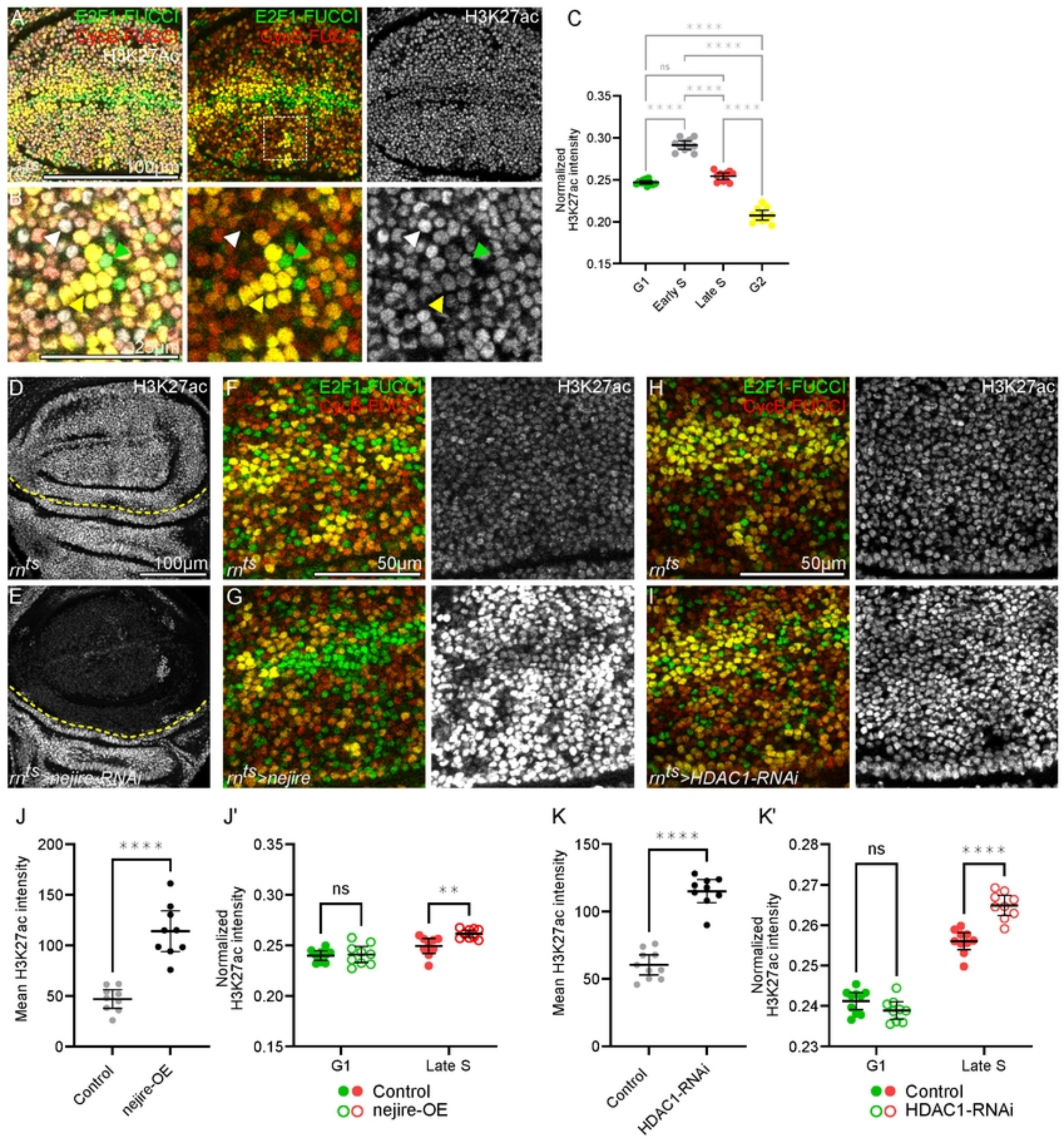

5

Main Figure 5

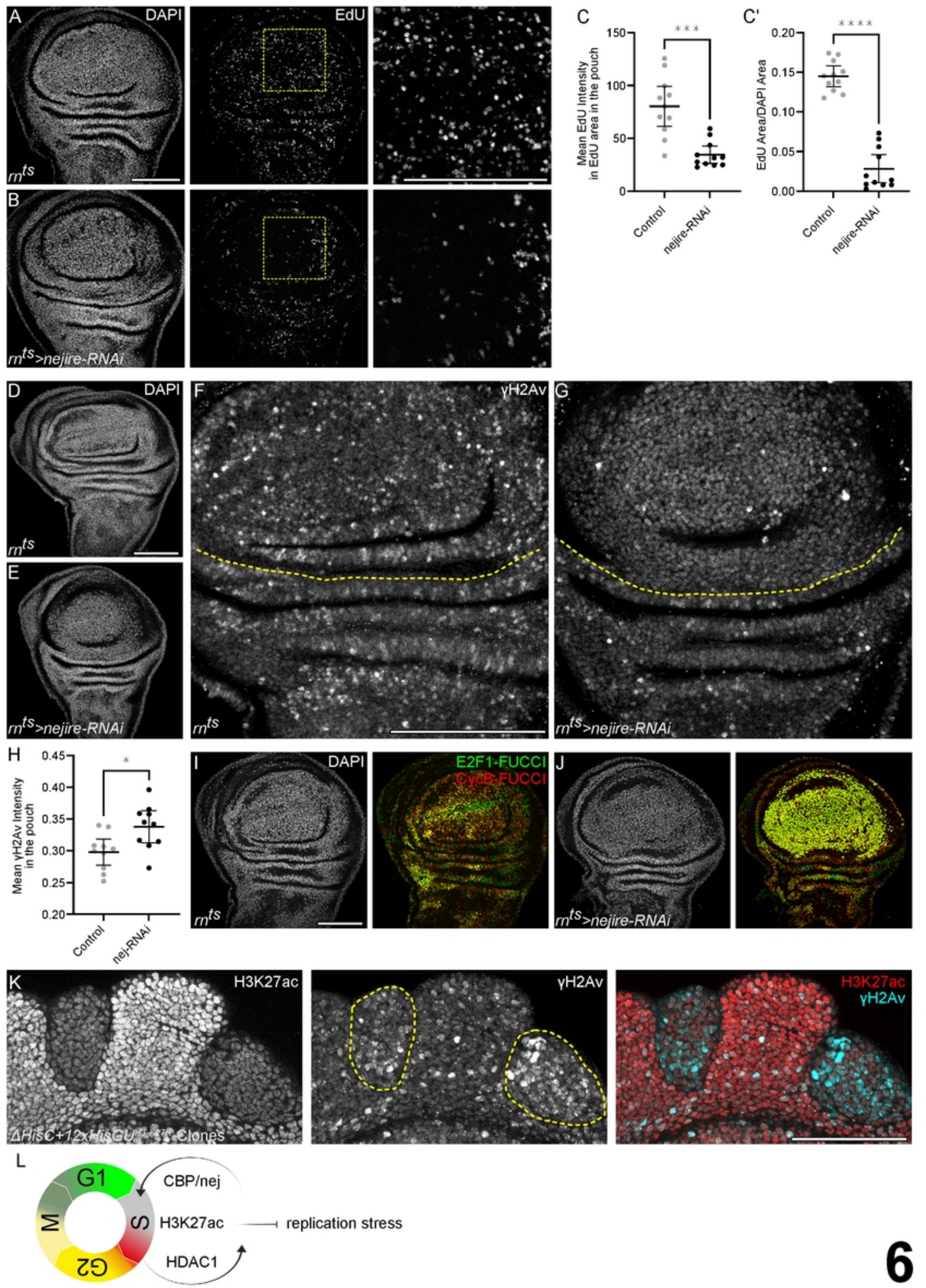

6

Main Figure 6